SLAC-PUB-2770
July 1981
(T/E)

DIRECT ELECTRON PAIR PRODUCTION IN $\pi^- p$ INTERACTIONS AT 16 GeV/c AND A MODEL FOR DIRECT LEPTON AND PHOTON PRODUCTION AT LOW P_T †

D. Blockus,[b] W. Dunwoodie,[a] D.W.G.S. Leith,[a] M. Marshall,[c] R. Stroynowski,[a] C. L Woody,[b] B. Barnett,[b] C. Y. Chien,[b] T. Fieguth,[a] M. Gilchriese,[a] D. Hutchinson,[a] W. B. Johnson,[a] P. Kunz,[a] T. Lasinski,[a] L. Madansky,[b] W. T. Meyer,[a] A. Pevsner,[b] B. Ratcliff,[a] P. Schacht,[a] J. Scheid,[c] S. Shapiro,[a] and S. Williams.[a]

SLAC[a] - Johns Hopkins[b] - Caltech[c] Collaboration

Abstract: The production of prompt electron-positron pairs in 16 GeV/c $\pi^- p$ collisions has been measured using the LASS spectrometer at SLAC. An excess of events is observed above the estimated contributions of direct and Dalitz decay of known resonances in the kinematic range defined by $0.1 \leq x \leq 0.45$, $0 \leq p_T \leq 0.8$ GeV/c and $0.2 \leq M(e^+e^-) \leq 0.7$ GeV/c^2. The excess signal decreases slowly with increasing M, but exhibits very steep x and p_T^2 dependence. The contribution of this signal to the $e^+e^-/\pi^+\pi^-$ and γ/π ratios is discussed. Detailed comparisons are made between e^+e^- distributions and the corresponding low mass $\mu^+\mu^-$ distributions, and a simple production mechanism is proposed which describes the 16 GeV/c data well. The implications for direct photon production are presented, and it is shown that the model provides simultaneously a good description of the experimental data on the (e/π) and (μ/π) ratios for $p_T < 1$ GeV/c.

---

† Work supported in part by the Department of Energy under contracts DE-AC03-76SF00515 (SLAC) and DE-AC03-76ER0068 (Caltech), and the National Science Foundation contract PHY-78-06917-A02 (Johns Hopkins).

a Stanford Linear Accelerator Center, Stanford University, Ca. 94305.

b Johns Hopkins University, Baltimore, Maryland 21218.

c California Institute of Technology, Pasadena, California 91125.

1. Introduction

Direct lepton pair production has received considerable attention in recent years [1]. The observed pair mass spectrum consists of vector meson contributions superimposed on a continuum which decreases rapidly with increasing mass. At high mass, the continuum is well-understood in terms of the Drell-Yan mechanism [2]. At low mass the data from $\mu^+\mu^-$ experiments [3-6] indicate that the signal below $\sim$1 GeV/c^2 is stronger than expected from vector meson decays alone, and is not compatible with the Drell-Yan description. There are also indications that the characteristics of the continuum depend on the kinematical range of observation. The inherently poor resolution of dimuon experiments has, however, made detailed study of the properties of the continuum difficult.

Low mass electron pair data are scarce and inconclusive. Two ISR experiments [7-8] have measured low mass e^+e^- pairs at large transverse momentum (p_T > 2 GeV/c); in each case the observed spectrum is consistent with the contributions resulting from Dalitz decay of η and ω mesons and semi-leptonic decays of charmed particles. Several bubble chamber groups [9-12] have seen indications of a low-mass continuum, but these experiments are limited by their low sensitivity.

Data on single lepton production for p_T < 1 GeV/c are also somewhat limited, and are usually presented in terms of the lepton to pion ratio. The (e/π) data result from pp interactions at $x \sim 0$ [13(a)-(c)] and indicate that the ratio increases exponentially with decreasing p_T, reaching a value of $\sim 6 \times 10^{-4}$ at p_T = 0.25 GeV/c [cf. Fig. 28]. In contrast, the muon data are obtained as averages over the low p_T

region at fixed x from proton-nucleus interactions, primarily in the 200 - 400 GeV/c incident momentum range [13(d)-(g)]. The (μ/π) ratio is observed to have a value $\sim 1.3 \times 10^{-4}$ at $x = 0$ and to decrease approximately exponentially with increasing x. [cf. Fig. 29]. Unanswered problems in this area involve the precise extent to which the single lepton distributions are a consequence of dilepton production [4, 13(e), 13(f)], and the simultaneous quantitative description of the observed (e/π) and (μ/π) behaviour.

The purpose of the present experiment is to address these questions by studying the direct production of electron pairs in $\pi^- p$ interactions at 16 GeV/c. The results on the mass, x and p_T^2 dependence have been published [14]. In chapters 2 and 3 the experimental procedure and results are discussed in detail, and in chapter 4 comparison is made between the e^+e^- data and corresponding $\mu^+\mu^-$ distributions. A simple model for the production mechanism is proposed in chapter 5, and its consequences for direct photon production and the behaviour of the single lepton to pion ratio at low p_T are presented.

2. The Experiment

2.1 Experimental Apparatus

The experiment was performed in a 16 GeV/c π^- beam at SLAC using the large aperture superconducting solenoid spectrometer, LASS [15]. Scintillation counter hodoscopes, two threshold Cerenkov counters and eight planes of 1 mm wire spacing proportional chamber were used to tag the incident pions and measure the momentum and trajectory of each beam particle incident on the 92 cm long liquid hydrogen target. The

beam particle parameters were determined to within ±0.25% in momentum, ±0.5 mrad in angle and ±1 mm in space at the interaction point.

The spectrometer is schematically represented in Fig. 1. It consists of a superconducting solenoid magnet vertex detector combined downstream with a large acceptance dipole magnet spectrometer. Small angle high momentum tracks are well measured in the downstream spectrometer, and the combination of the two detector systems provides $\sim 4\pi$ geometrical acceptance for charged particles as well as good momentum resolution over a wide range of longitudinal and transverse momenta. A detailed description of the various detector components is to be found in reference 15.

The vertex spectrometer has an approximately uniform field of 22.4 Kgauss parallel to the incident beam direction in a volume of 1.9 m diameter and 4 m length. The target occupied the first ~1 m of the field region and was surrounded by a cylindrical multiwire proportional chamber and 15 planes of cylindrical spark chambers providing stereo measurement of azimuth and z coordinate for particles exiting the target at large angles. Downstream of the target there were three 1 mm wire spacing capacitive diode readout (CD) spark chambers (four planes per chamber), two MWPC's with 2 mm wire spacing (three planes per chamber), and three MWPC radial hodoscopes (with 1.4° azimuthal angle resolution) covering the full aperture of the solenoid. The spark chambers were deadened in the central region by 21.6 cm diameter polyurethane discs and these regions were read out by 1 mm wire spacing MWPC's mounted on the mechanical frames of the spark chambers. These assemblies provided ~0.5 mm spatial resolution over the full 2 × 2 meters

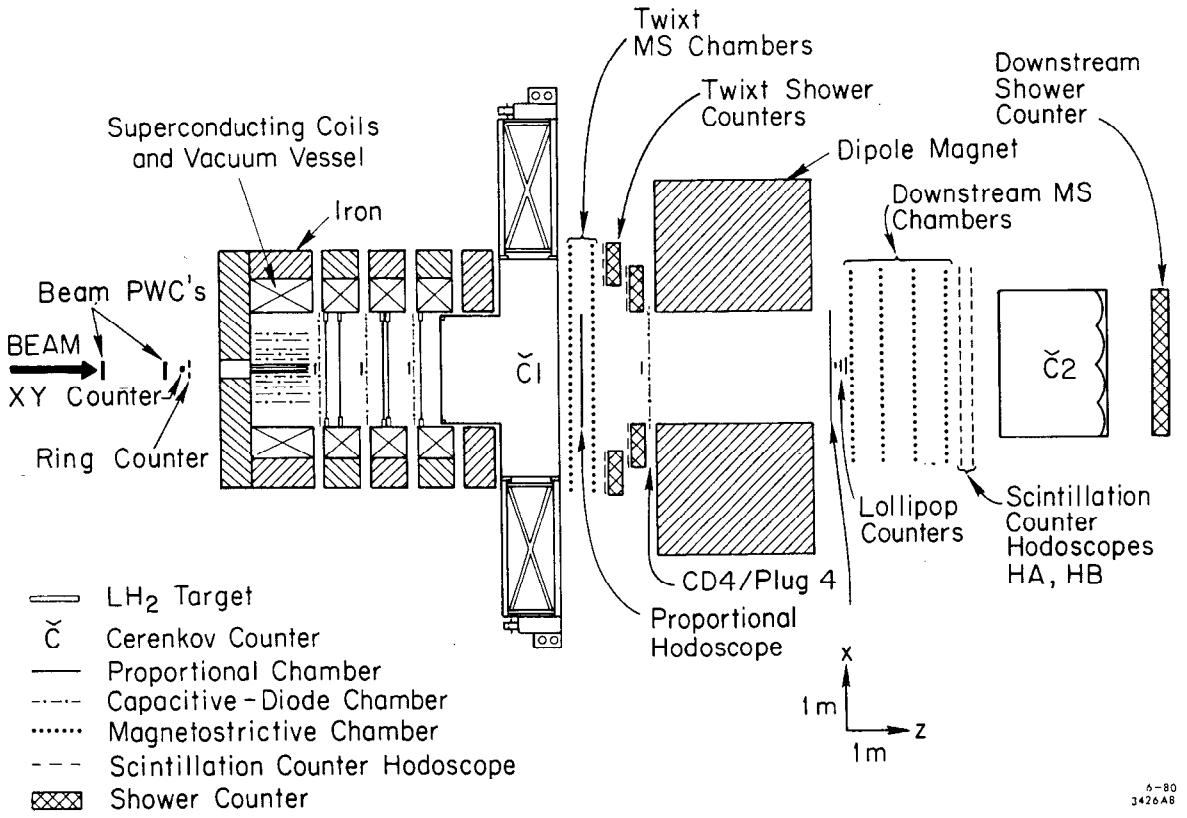

Fig. 1. The LASS spectrometer layout (plan-view).

active areas of the chambers combined with short memory time (~50 nsec) in the busy central region. The end of the solenoid was closed by a 38 cell threshold Cerenkov counter filled with air at atmospheric pressure. Under these conditions, the Cerenkov threshold for electrons was 21 MeV/c and for pions it was 5.8 GeV/c. The lower quadrant of 9 cells was not instrumented during this experiment.

The forward spectrometer was built around an analyzing magnet with 2 × 1 meter gap and 32 Kgauss-meter field integral. Upstream, there were two (5 × 2) meter magnetostrictive (MS) spark chambers with four readout planes each, a capacitive diode readout spark chamber with central MWPC assembly (as described above for the vertex spectrometer) and a (2.5 × 2) meter MWPC hodoscope with 4 mm wire spacing. Finally, there were 13 total absorption shower counters ≈15 radiation length thick, arranged around the magnet aperture (Fig. 2). They consisted of alternating layers of doped lucite and lead convertor plates of varying thickness chosen to provide uniform pulse height response over the entire area of the counters. A layer of scintillation counters placed in front of each shower counter provided a gamma veto by recording the passage of charged particles. Downstream, there were four magnetostrictive readout spark chambers (3 × 1.5) meters in area, each with four planes of readout, and a 4 mm wire spacing MWPC hodoscope of (2.5 × 1.5) meters. In-time information for track reconstruction was provided by the MWPC hodoscopes and two arrays of scintillation counters located immediately behind the spark chamber package. Finally, a second threshold Cerenkov counter and a lead-scintillator sandwich shower counter completed the forward system. The detector lever arm upstream of the analyzing magnet

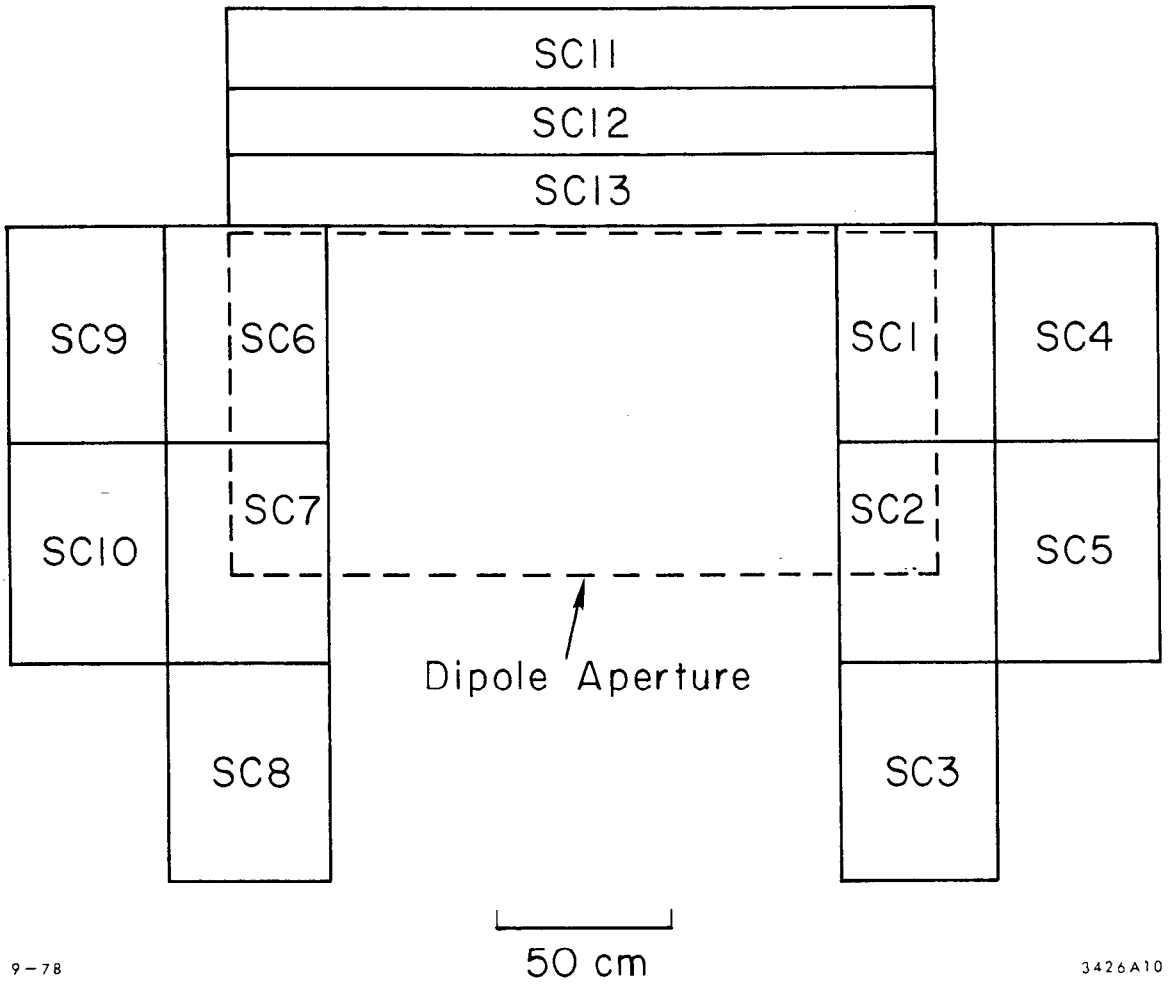

Fig. 2. The shower counter arrangement around the aperture of the dipole magnet.

was 0.8 meters and downstream it was 1.7 meters, yielding momentum resolution of better than 0.5 percent for forward particles. The resolution of the spectrometer may be characterized by the following: the $K^o \to \pi^+\pi^-$ invariant mass resolution is 14 MeV FWHM, the production angles of charged particles are measured to ±0.6 mrad and the missing mass resolution for a recoil baryon is typically ~±70 MeV. The reconstruction of zero-opening angle γ conversions is complicated by the problem of the granularity of the measurements which increases the γ mass resolution from the expected 10 MeV to ~30 MeV. Nevertheless, the $\gamma\gamma$ effective mass reconstructed from 4 electron tracks (Fig. 3) shows a clear π^o peak of 28 MeV FWHM.

The trigger for the experiment was designed to select events with at least one electron present. It required a coincidence among an identified incident π^-, one or more cells in the Cerenkov counter, C1, and one or more of the shower counters with its attendant γ-veto counter. The resulting trigger rate was ~5.5 10^{-3} per incident pion. Additional triggers were mixed in with this electron trigger to provide samples of events for study of the performance of the spectrometer. These extra data came from an interaction trigger--which sampled the total cross section--and from non-interacting beam particles--which were used to determine the beam profile characteristics throughout the experiment.

2.2 Acceptance and Performance of the Spectrometer

The geometrical acceptance of LASS for the reconstruction of charged tracks covers essentially the full 4π solid angle. The acceptance for direct electron pair production is defined by the

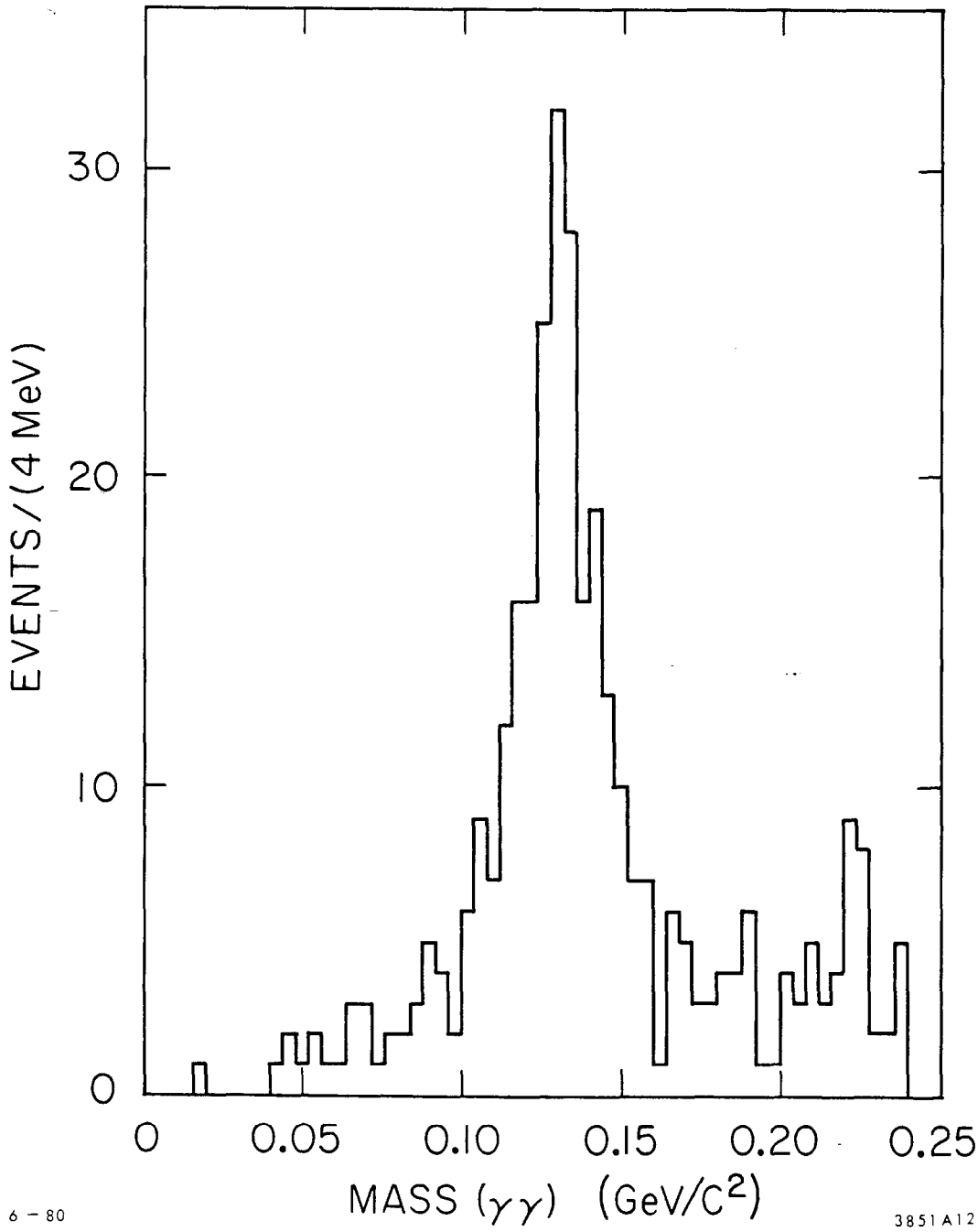

Fig. 3. The two photon effective mass distribution in the vicinity of the π^0 from a sub-sample of the data.

geometry and electron identification capabilities of Cerenkov C1 and the shower counter system.

The threshold for pions to produce light in C1 was approximately 5.8 GeV/c. In order to remove problems related to the momentum resolution and edge effects in the extrapolation of the measured tracks through the inhomogeneous fringe field region between the end of the solenoid and the shower counters, an upper limit of p_{LAB} = 5.0 GeV/c was imposed on electron track candidates during the off-line analysis. The hadron rejection of C1 was measured in a test arrangement to be better than 5.10^{-4} per track. The efficiency of the counter for identifying electrons depended on the momentum and emission angle of the tracks. In order to estimate the C1 efficiency in the experimentally covered kinematical range, a sample of converted photons was selected having one track doubly-identified by C1 Cerenkov and a shower counter, and with reconstructed effective mass of the photon less than 50 MeV. The second track of the pair assured an unbiased measurement of efficiency and the results are shown in Fig. 4(a) as a function of track momentum. A similar procedure resulted in the estimates of the efficiencies of the shower counters shown in Figs. 4(b) and 4(c) [15].

The drop in C1 efficiency at low momentum was due to increased spiralling of the charged track in the solenoid's magnetic field, which resulted in a shorter path-length in any individual C1 cell.

The decrease of shower counter efficiency at low momentum resulted from the imposed threshold pulse height cuts for electron identification. These cuts gave a hadron misidentification probability which was typically ~13%, so that the combined Cerenkov and shower counter hadron rejection was better than 6×10^{-5} per track.

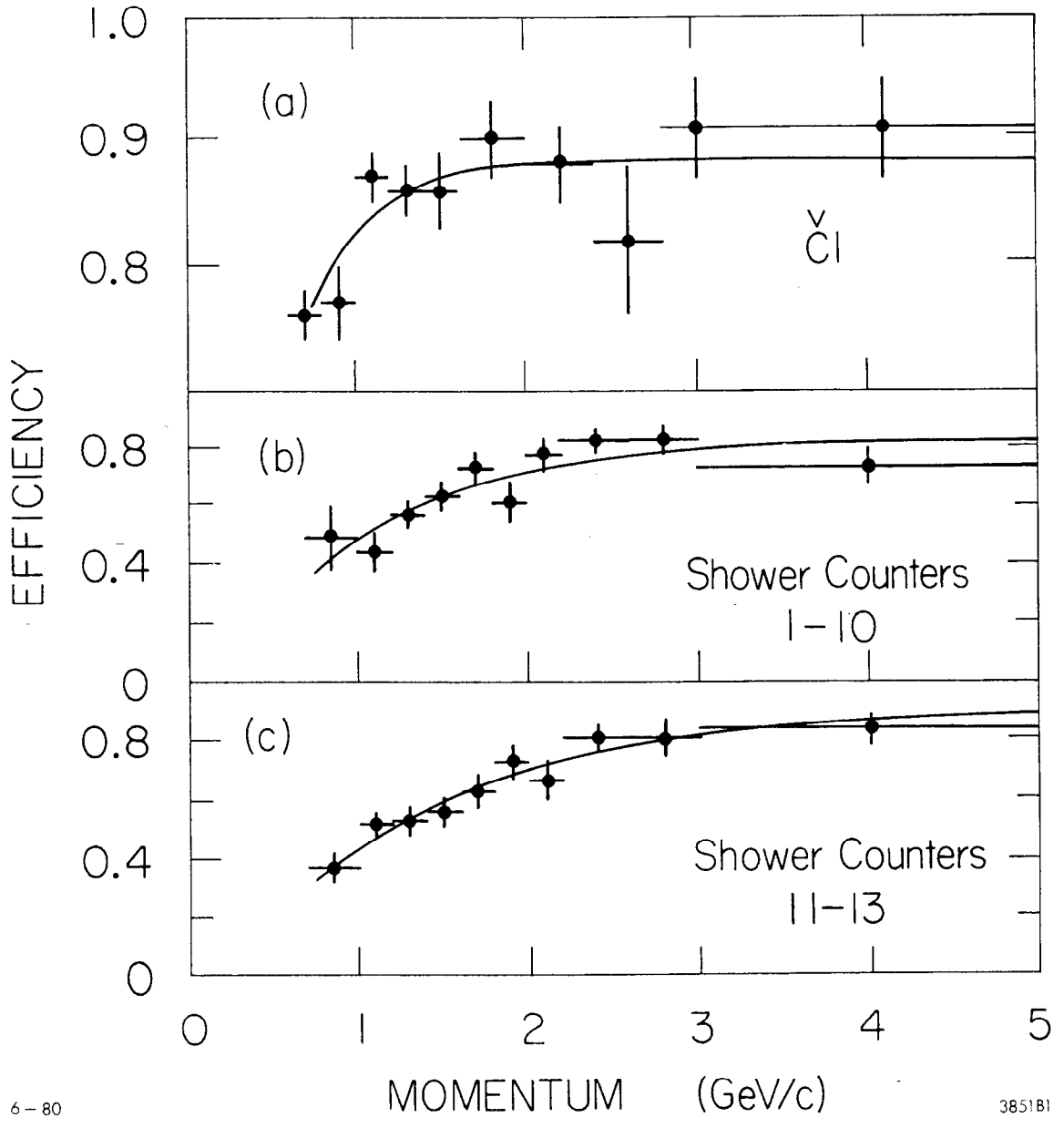

Fig. 4. The electron identification efficiency as a function of particle total momentum for a) Cerenkov counter C1, b) shower counters 1-10 and c) shower counters 11-13.

Due to the sharp drop of efficiency at small momenta, the lower limit for electron identification was set at $p_{LAB} = 0.75$ GeV/c.

The geometrical acceptance for pairs of electrons with individual tracks in the $0.75 \leq p_{LAB} \leq 0.5$ GeV/c momentum range was calculated by a Monte Carlo method using a realistic description of the apparatus and the geometry of the counters. The acceptance is in general a function of x, p_T and pair mass M, as well as the internal angular variables describing the e^+e^- system. In all subsequent discussion of acceptance it is assumed that the electron angular distribution is isotropic in the pair rest frame. With this assumption, the acceptance may be evaluated at any point in (x, p_T, M) space, and, as discussed in Section 2.2 below, such a procedure was followed during the analysis of the data. However, in order to demonstrate the general acceptance characteristics for electron pairs as a function of pair mass, it is necessary to make use of a model for the (x, p_T) dependence of the cross section. The geometrical acceptance shown by the dot-dashed curve in Fig. 5 was calculated under the assumption that at all masses the x and p_T dependence is the same as that of the ρ^o produced in $\pi^- p$ interactions at 16 GeV/c [16(a)]. The dashed curve in Fig. 5 shows the same acceptance taking into account the efficiency for electron identification.

The overall acceptance of the experiment involves, in addition, efficiencies of the chambers and of the pattern recognition programs. In order to include these effects a special Monte Carlo program was set up which tracked the individual charged particles through LASS and generated individual hits according to the measured hardware efficiency and spatial resolution for each detector plane. These coordinates were

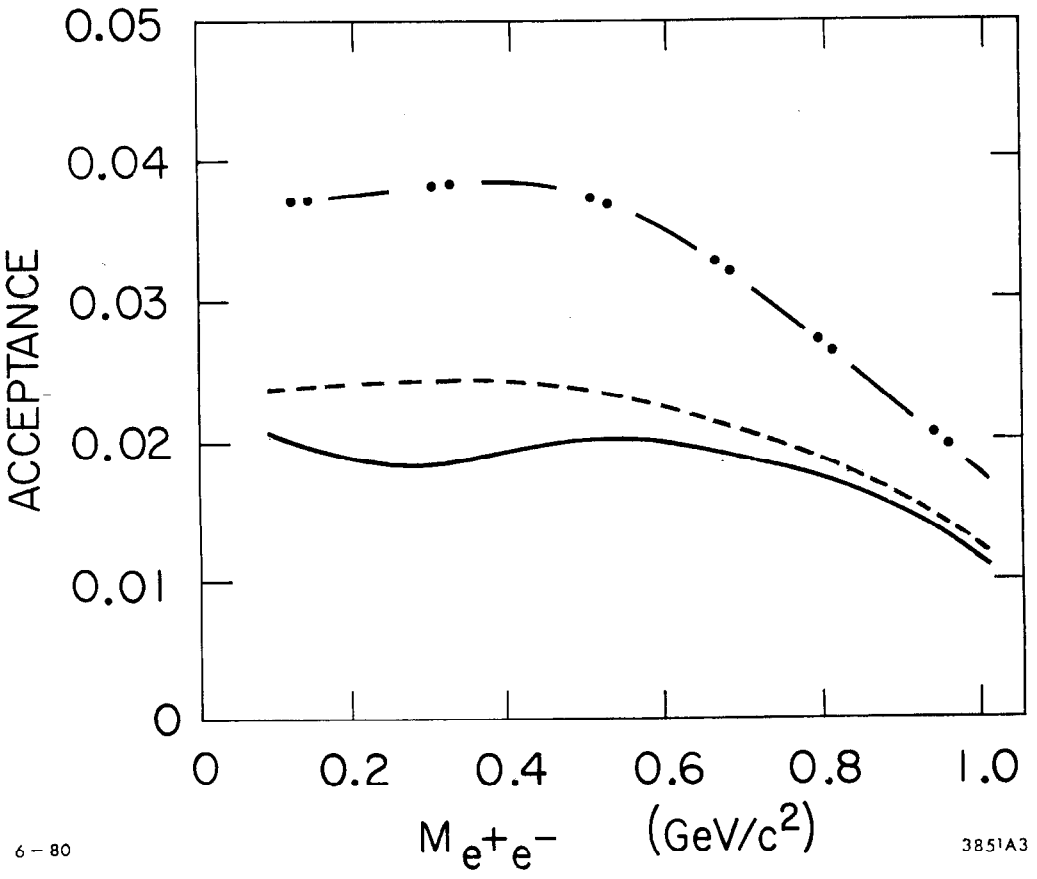

Fig. 5. The acceptance as a function of $M(e^+e^-)$ for the isotropic decay of e^+e^- pairs produced with the (x, p_T^2) dependence of the ρ^o. The dotted-dashed line describes the geometrical acceptance, the dashed line includes in addition the electron identification efficiencies and the solid line represents the overall acceptance after the pattern recognition efficiency has been included.

then collected to form an input data buffer acceptable to the production version of the data processing program. The comparison of the output from this process with the original input provided a measure of the overall software efficiency. As a test of the procedure, the data from the 16 GeV/c $\pi^- p$ bubble chamber experiment [17] were used for comparison with a sample of the total cross section trigger data from this experiment. The comparison presented in Fig. 6 shows that the above procedure very well describes in absolute normalization the efficiency of the LASS apparatus and software system as a function of the momentum of the produced particles.

When the hardware and software efficiency is incorporated into the Monte Carlo calculations the resulting mass dependence of the overall acceptance is as shown by the solid curve in Fig. 5.

2.3 The Data

The loose trigger described above yielded about 5.1×10^6 events written to magnetic tape for an incident flux of $\sim 10^9$ pions. In order to avoid unnecessarily large computing time, an off-line selection of events was performed. The selection required that at least one pair of signals from the shower counters and individual C1 cells satisfy a C1-shower counter correlation pattern developed for reconstructed tracks with laboratory momentum above 0.75 GeV/c. In addition, as a minimal condition for the presence of an electron pair, a signal was required in a second cell of the C1 Cerenkov counter. This pre-selection reduced the data sample by about a factor of five. The remaining ~900 k events were processed through the pattern recognition program requiring

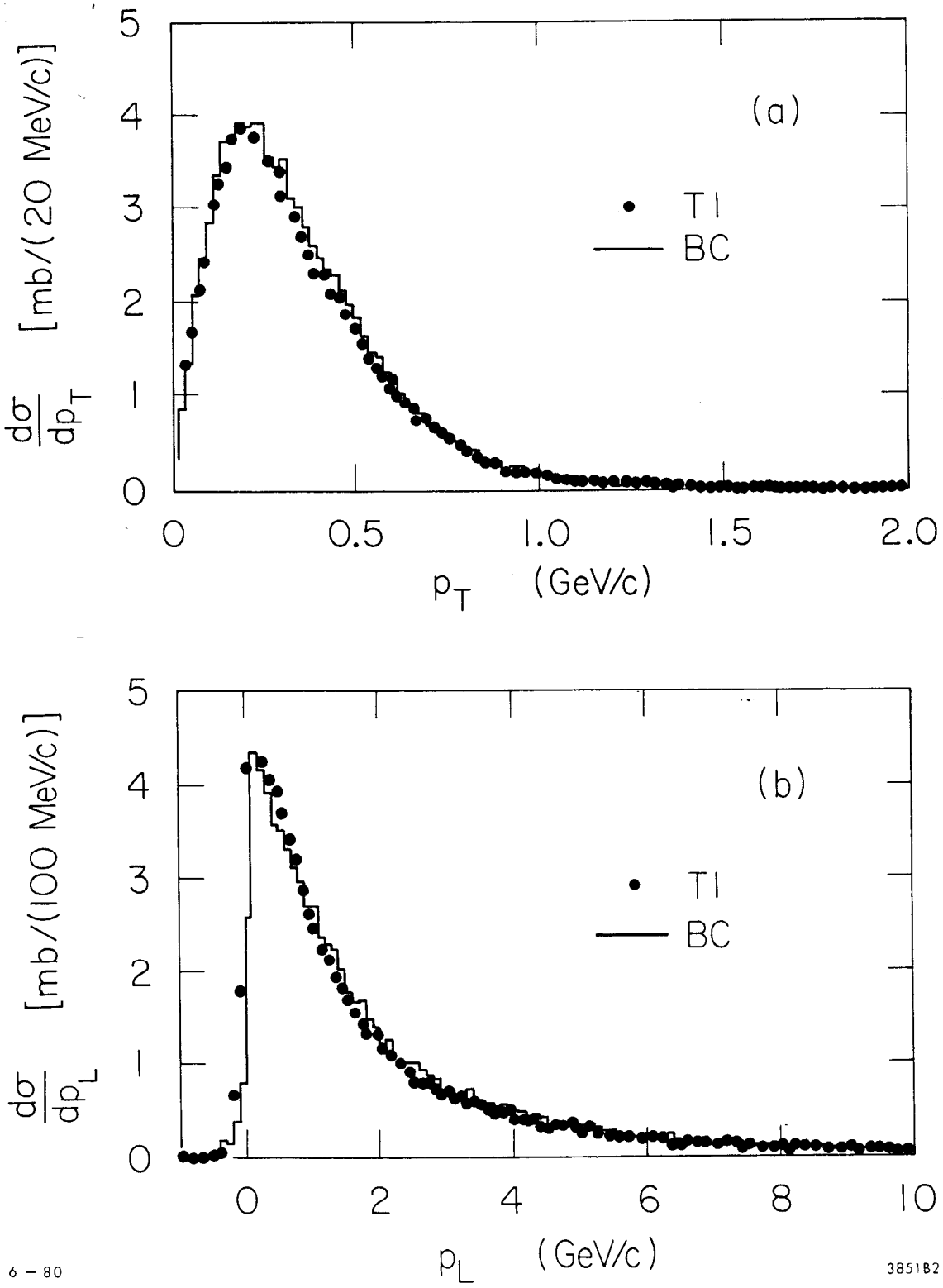

Fig. 6. A comparison of the 16 GeV/c π^-p bubble chamber data (histogram) with the total cross section trigger from this experiment (dots).

reconstruction of a triggering electron track(*) with $p > 0.75$ GeV/c and at least one other electron candidate; the second electron candidate could be identified on the basis of C1 alone, but not on the basis of a shower counter alone. Furthermore, it was required that the second track turn on at least one C1 cell which was not on the triggering electron track. The resulting ~112 k events were dominated by photon conversions away from the primary vertex. For a fraction of the data the electron pair was fitted to a two particle vertex independently of the remaining tracks in the events, and the remaining tracks fitted with the beam track to form a primary vertex. Figure 7 is a scatter diagram of the distance between the primary and electron pair vertices versus the mass of the pair. Direct pair candidates comprise the narrow vertical band. The horizontal band corresponds to photon conversion. The fact that this band extends to negative values of the distance together with a corresponding increase of effective mass indicates the problems of resolution for small opening angle (i.e., low mass) electron pairs. A mass cut at 200 MeV effectively eliminates these problems. The remaining pair candidates are highly correlated with the primary vertex; this clearly shows that any high mass signal cannot be construed to result from badly-measured γ-conversions.

The mass cut at 200 MeV also eliminates contributions from the tail of the π^o Dalitz decay distribution, since the pair mass resolution near the π^o mass is ~12 MeV [of Fig. 3]. This selection, together with the requirement that the electron pair form a good vertex with the beam track

---

(*) A triggering electron is required to be identified in <u>both</u> C1 and the shower counter wall.

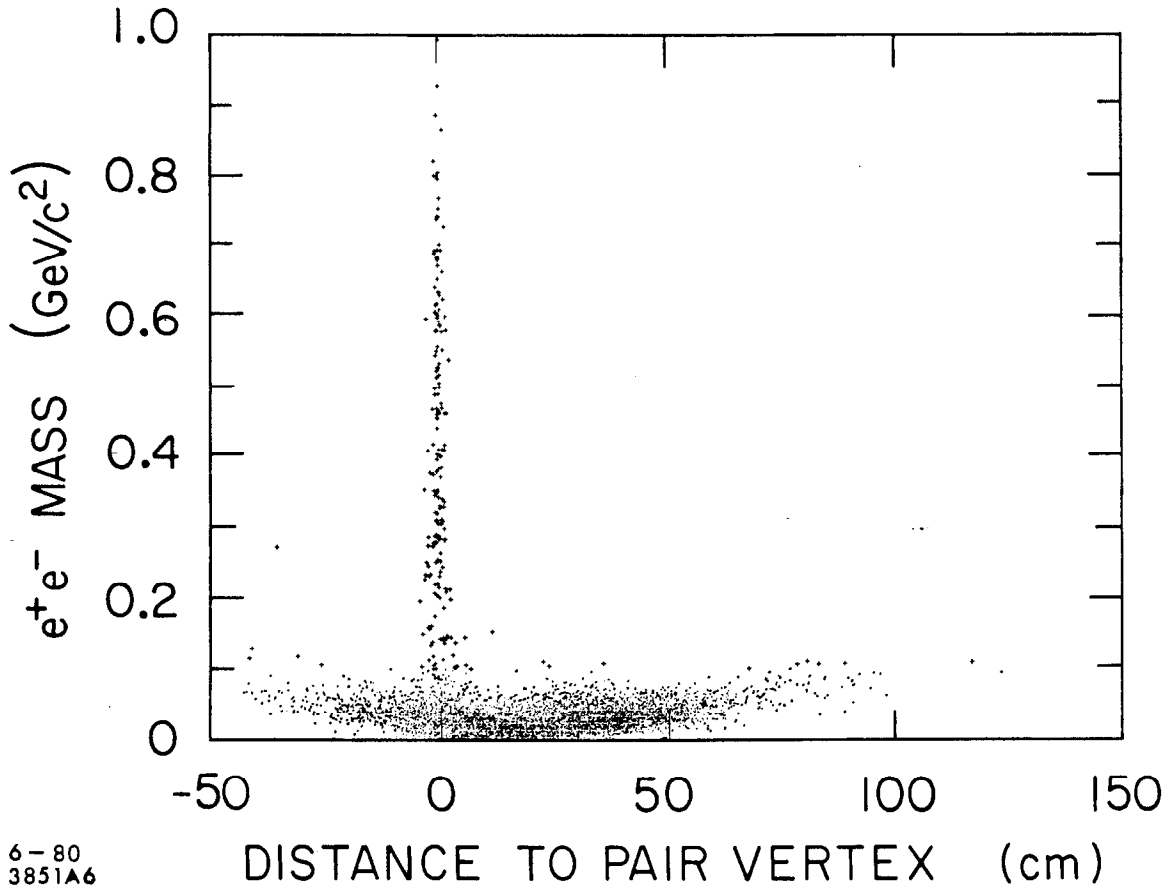

Fig. 7. The distance from the primary to electron pair vertex versus the mass of the pair. The darkness of points is enhanced for masses above 100 MeV/c^2.

yields a sample of 1811 events having at least one direct electron pair candidate containing a triggering track. It should be emphasized that the entire selection process was carried out without regard to the net charge of the candidate electron pair. This was done so that an unbiased estimate of background contributions to the final e^+e^- sample could be obtained.

The major source of background among the remaining events is due to the case in which two photons convert into e^+e^- pairs, typically with highly-asymmetric energy partition, and one electron of each pair is not reconstructed. The process of elimination employed in defining this sample had in effect led to an increased concentration of events suffering from hardware inefficiency problems. Therefore, a special version of the pattern recognition program was employed in reprocessing these remaining events in which track definition criteria were relaxed. Such procedures could not be employed in the production version of the software since they significantly increased the processing time per event.

All 1811 events were reprocessed and then individually scanned by physicists. The initial sample of 1811 events contained an excess of ~100 opposite sign over same sign pairs. The scanning procedure resulted in a final data sample of 291 events in the phase space volume defined by

$$0.2 \leq M \leq 1.2 \text{ GeV/c}^2$$

$$0.10 \leq x \leq 0.45$$

$$0.0 \leq p_T \leq 0.8 \text{ GeV/c} \quad ;$$

this final sample shows an excess of 107 opposite over same sign pairs, so that this final stage of event selection resulted in a dramatic reduction in background while having no significant effect on the magnitude of the opposite sign signal. Of the remaining events, about 90% contain one and only one candidate pair; for the other events, each pair was given weight equal to the inverse of the total number of candidate pairs in the event.

3. Results

3.1 Background

In Figs. 8 and 9 are shown the M, x and p_T^2 spectra for the opposite and same sign electron pair samples defined as described in Section 2. Although the M and x distributions are rather similar in shape for both charge combinations, it should be noted that the p_T^2 spectra are markedly different at low p_T^2.

The same sign electron pair background consists of pairs of three types:

(i) pairs formed by electrons originating from different conversions;

(ii) pairs containing an electron from a γ-conversion and a misidentified hadron;

(iii) pairs containing two misidentified hadrons.

Categories (i) and (ii) contribute equally to the same and opposite sign pair samples since the probability of finding only one electron from a γ-conversion is charge symmetric.

This is not the case of category (iii), however, and in fact, the 16 GeV/c $\pi^- p$ bubble chamber data [17] show that the inclusive cross

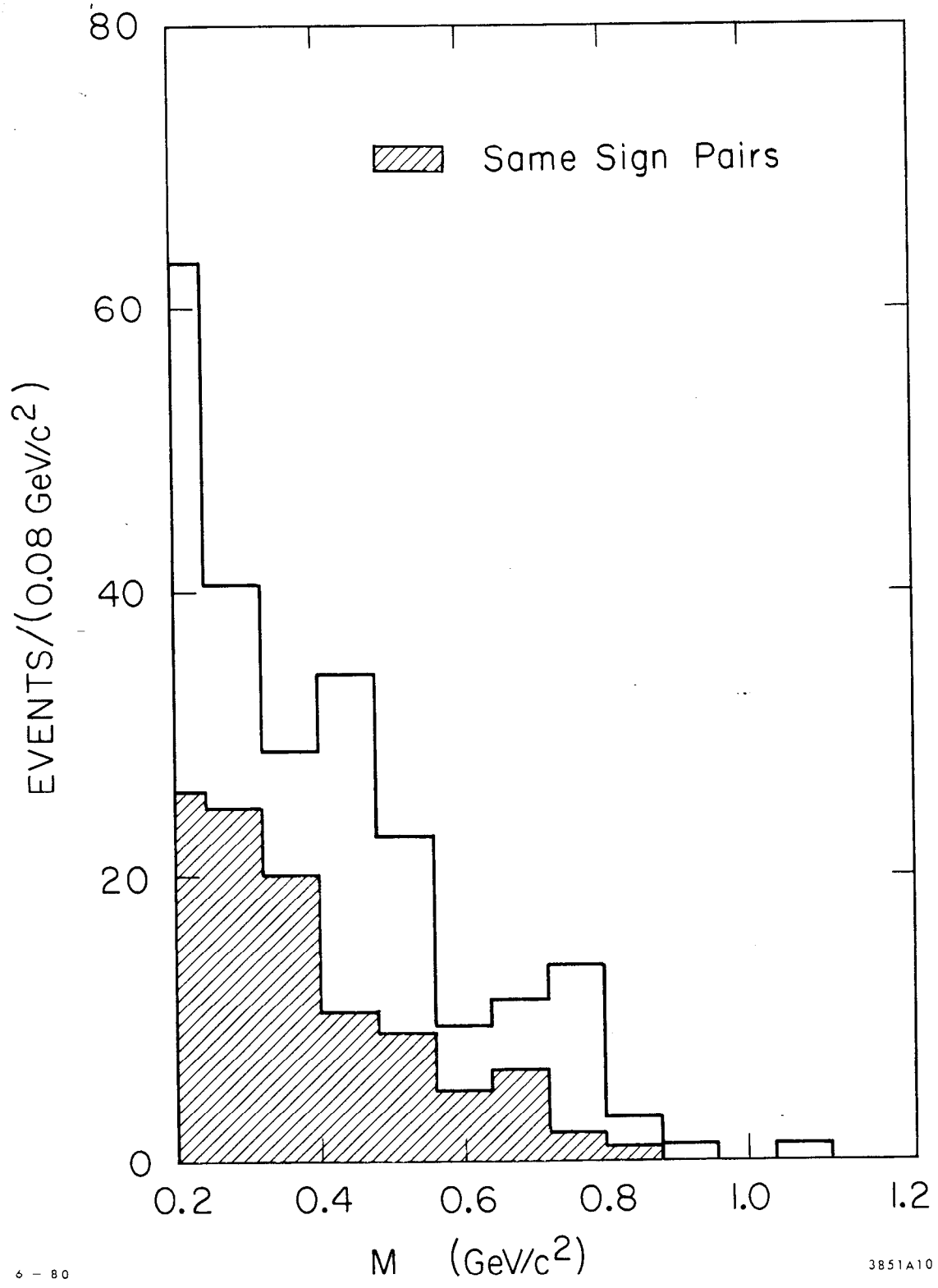

Fig. 8. The uncorrected mass distributions of opposite and same sign electron pairs.

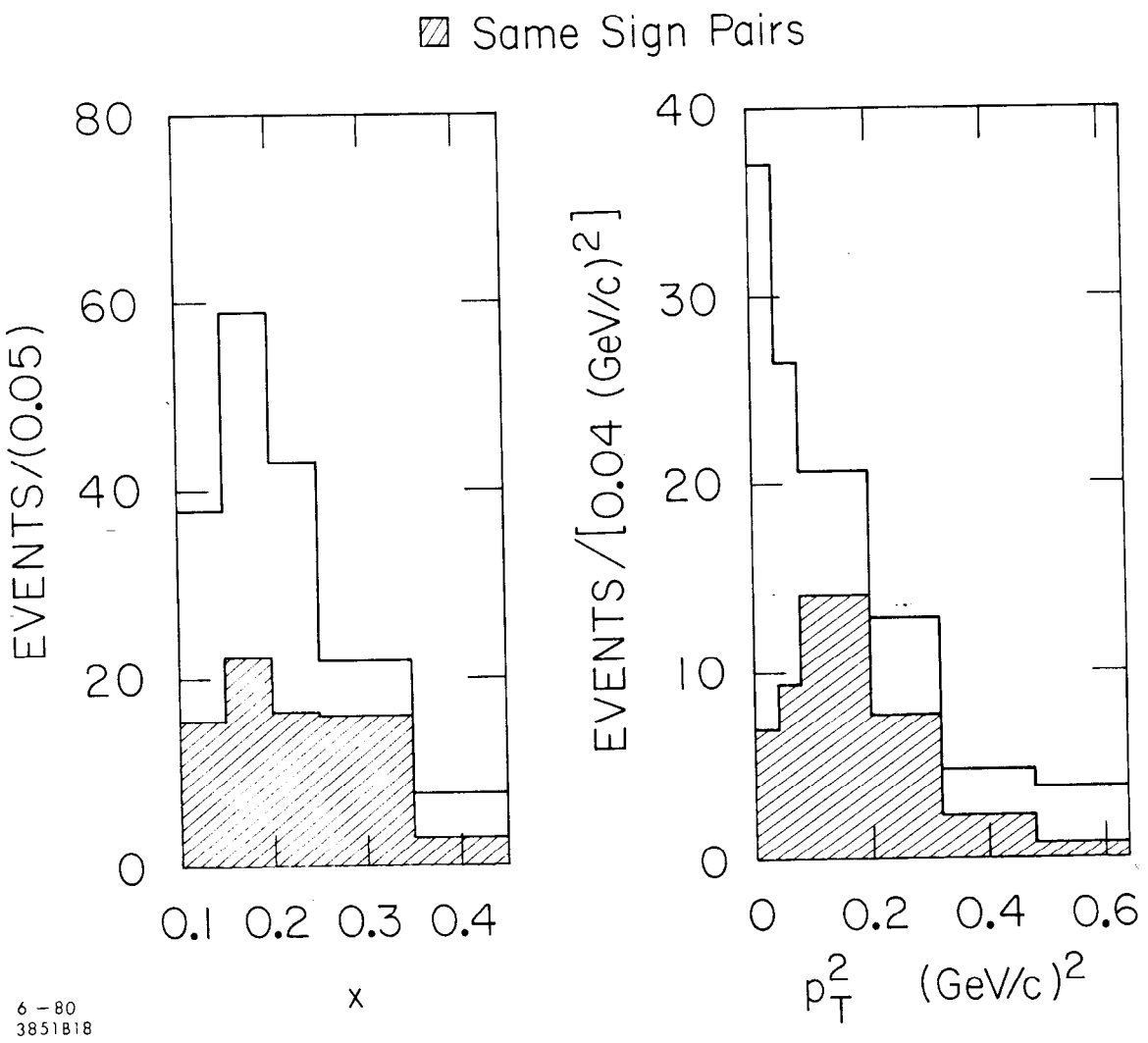

Fig. 9. The uncorrected x and p_T^2 distributions of opposite and same sign electron pairs.

section for same sign hadron pairs is only ~60% of the opposite sign pair cross section.

In this experiment the probability for a hadron to fire a C1 cell is negligibly small for $0.75 \leq p \leq 5.0$ GeV/c; however, a hadron may be misidentified because an electron which traversed the same C1 cell was not reconstructed by the track-finding program. An estimate of the consequent hadron-hadron contribution to the direct electron pair sample was obtained as follows. For each cell of C1 the probability of observing a signal with no corresponding track found was measured using the total interaction trigger data. The obtained values together with the average hadron misidentification probability of the shower counters were incorporated as efficiencies into the Monte Carlo program. Using the multiparticle distributions of the bubble chamber experiment [17] to measure the dihadron background in the direct sample, an estimated contribution of (6 ± 4) events was obtained.

The difference between the opposite and same sign pair mass spectra of Fig. 8 is shown in Fig. 10, together with the estimated dihadron background. The direct e^+e^- pair sample contains (107 ± 17) events yielding a net <u>observed</u> e^+e^- pair cross section of (45 ± 7) nb.(*)

The corresponding subtracted x and p_T^2 distributions are shown in Fig. 11. The x distribution shows a dramatic increase for $x \leq 0.25$ and and equally striking effect is observed in the p_T^2 distribution for $p_T^2 \leq 0.1$ (GeV/c^2). These features will be discussed in more detail in subsequent sections.

(*) The incident flux of ~10^9 π^-p results in a sensitivity of 2.4 events/nb.

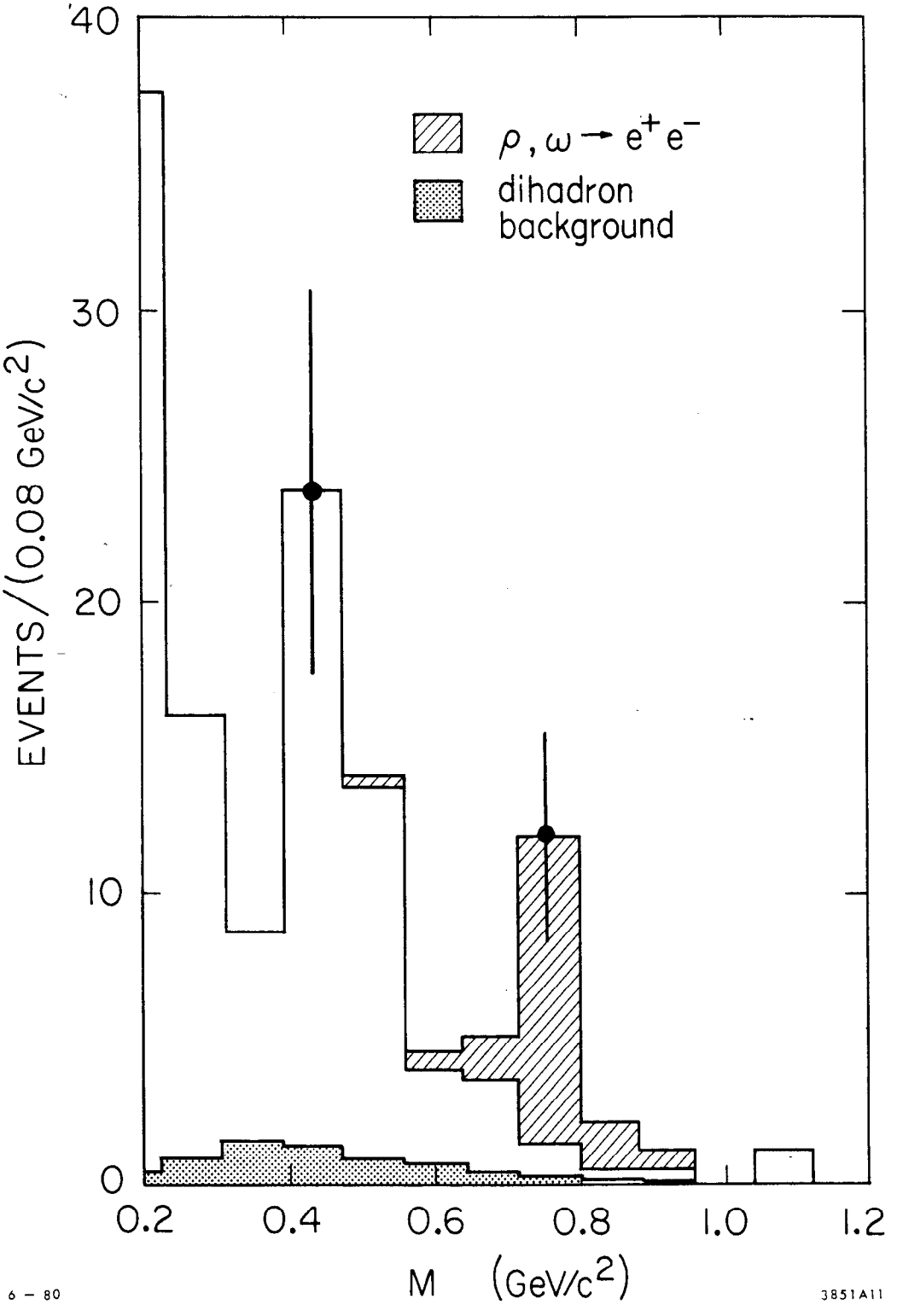

Fig. 10. The mass distribution of direct e^+e^- pairs. The estimated contributions of dihadron background and direct decays of ρ^o and ω mesons are shown as shaded areas.

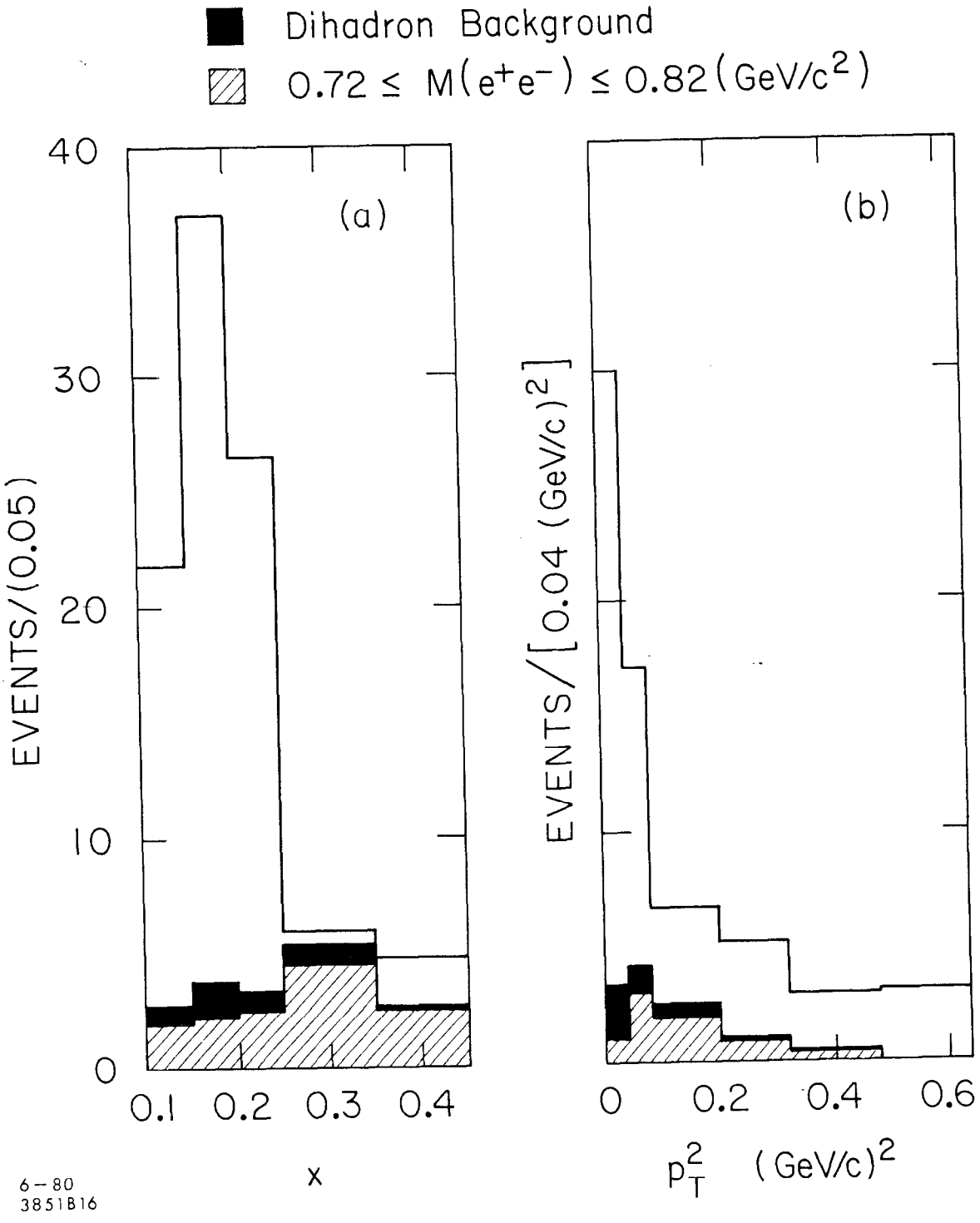

Fig. 11. The x and p_T^2 distributions of direct e^+e^- pairs. The contributions of dihadron background and direct decays of ρ^o and ω mesons are shown as shaded areas.

3.2 Direct ρ and ω Decay to e^+e^-

In the mass interval 0.72 - 0.80 GeV/c^2 of Fig. 10 there are 11.8 ± 3.8 events with virtually no dihadron background. It is natural to associate this signal with the production of the ρ and ω resonances and their subsequent decay to e^+e^-.

In order to estimate the expected contribution from such a mechanism Monte Carlo calculations were performed using the estimated ρ^o and ω production cross sections in π^-p interactions at 16 GeV/c [16]. As indicated in Section 2.2, these calculations took into account geometrical acceptance, software and electron identification efficiencies. Using decay branching ratios from the Particle Data Tables [18] and the sensitivity of the experiment (2.4 events/nb) the spectrum of Fig. 10 is expected to contain (7.5 ± 0.6)ρ^o events and (7.5 ± 2.0)ω events, ignoring possible interference effects. As indicated in Fig. 10, such a contribution is completely consistent with the observed e^+e^- mass spectrum.

The contribution from the ρ-ω region to the x and p_T^2 distributions is shown in Fig. 11. It is clear that the sharp increases in the low x and the low p_T^2 regions are characteristics of the low mass e^+e^- continuum and differ markedly from the direct decay distributions of the ρ and ω resonances.

3.3 The Low Mass Continuum

The low mass continuum is defined by the mass selection

$$0.2 < M(e^+e^-) < 0.7 \text{ GeV}/c^2 \quad .$$

The net e^+e^- sample corresponding to this interval consists of (92 ± 16)

events, and contains ~1 $\rho \to e^+e^-$ event in addition to the estimated (6 ± 4) events hadron-hadron contamination.

The remaining major contribution from known sources in the low mass region is due to Dalitz decay of η and ω mesons:

$$\eta \to e^+e^- \gamma$$

$$\omega \to e^+e^- \pi^o \quad .$$

A similar Monte Carlo technique to that described in Sections 2.2 and 3.2 was used to estimate the contributions from these processes. The η production was assumed to have the same x and p_T dependence as ω production [16b], and the parent meson was assumed to decay isotropically in its rest frame into an e^+e^- subsystem of mass M and the recoil particle; the subsystem M was then assumed to decay as $(1 + \cos^2\theta)$ in its rest system. The functions describing the distribution in M were taken from references [19] and [20] for η and ω respectively, with corresponding branching ratios of 5.0×10^{-3} [18] and 8.0×10^{-4} [20] for the Dalitz processes.

The resulting η and ω contributions to the low mass continuum are estimated to be (15.3 ± 5.3) and (10.3 ± 1.6) events respectively; the errors correspond to the uncertainties in the values of the inclusive η and ω cross section at 16 GeV/c. It follows that these sources account for only ~30% of the observed direct signal.

The M, x and p_T^2 distributions for the low mass continuum are shown in Fig. 12 together with the estimates of the corresponding η and ω Dalitz decay contributions. It is clear that the dynamical characteristics of the excess events are quite different from those of the η and

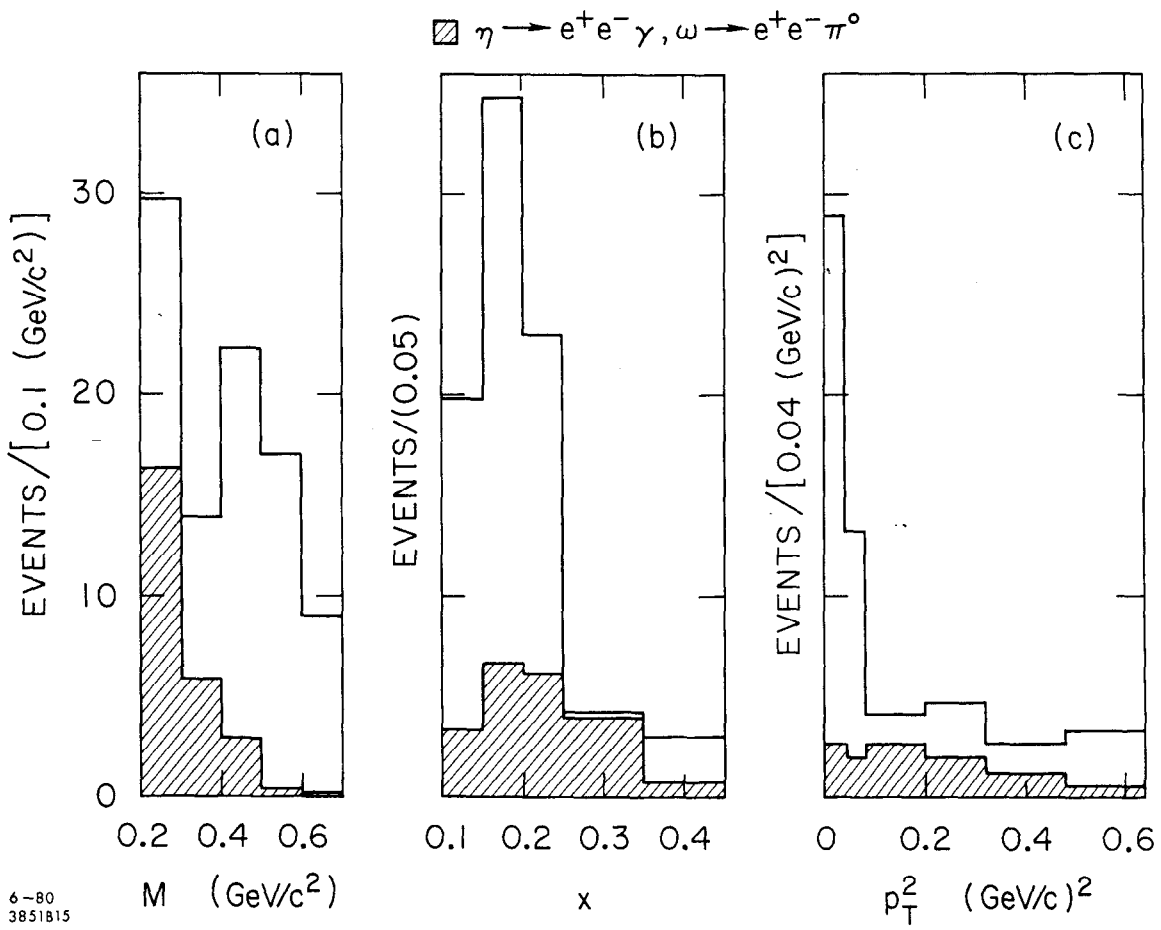

Fig. 12. The uncorrected distributions of mass, x and p_T^2 for the continuum. The estimated contributions of η and ω Dalitz decays are shown as shaded areas.

ω spectra. The mass distribution (Fig. 2(a)) is varying more slowly, whereas the x and p_T^2 distributions are much steeper for $x \leq 0.25$ and $p_T^2 \leq 0.1$ $(GeV/c)^2$ respectively.

The low mass continuum contains (66 ± 17) events in excess of the estimated η and ω contribution, and (59 ± 17) events when all known sources of background are removed.

3.4 Acceptance-Corrected Continuum Distributions

In order to obtain corrected cross sections and distributions for the low mass continuum it is necessary to have a representation of the overall acceptance at each point of the (x, p_T^2, M) phase space volume accessible to the experiment. Using the Monte Carlo program, the overall acceptance of the experiment has been estimated on a grid spanning this phase space under the assumption that the e^+e^- pair internal angular distribution is isotropic. A linear interpolation procedure was then used to evaluate the acceptance for each event of the data sample. Each pair was weighted by the inverse of its acceptance value,(*) same sign pairs being given negative weight. The corrected cross section for the low mass continuum is found in this way to be (955 ± 170) nb. The estimated (η, ω) contribution is (255 ± 60) nb, so that the excess corresponds to a cross section of (700 ± 180) nb in the acceptance region of the experiment.

(*) Acceptance values are almost entirely in the range 5 - 17% with a tail extending to ~1%.

In Figs. 13(a)-(c) are shown the acceptance corrected M, x and p_T^2 distributions of the continuum,(*) and in Figs. 13(d)-(f) these distributions are reproduced after subtraction of the estimated η and ω contributions.

Describing the mass spectra by the parametrization:

$$\frac{d\sigma}{dM} = C_1 M^{-\alpha}$$

α is found to be $\alpha = 1.77 \pm 0.64$ for Fig. 13(a) and $\alpha = 0.94 \pm 0.89$ for Fig. 13(d). The removal of the estimated (η, ω) contribution results in a residual mass spectrum which is consistent with an M^{-1} dependence.

Fits to the x distributions (Figs. 13(b), (e)) of the expression

$$\frac{d\sigma}{dx} = C_2(1 - x)^{\beta}$$

yield $\beta = 7.46 \pm 1.72$ and $\beta = 9.78 \pm 2.64$ for the unsubtracted and subtracted distributions, respectively. In this case, removal of the η and ω contributions yields a somewhat steeper x dependence for the continuum excess.

The p_T^2 distributions of Figs. 13(c) and (f) are not well described by a single exponential function. Furthermore, for the unsubtracted data:

$$\langle p_T^2 \rangle = 0.137 \pm 0.034 \ (\text{GeV/c})^2 \quad \text{for } 0.10 \leq x \leq 0.20$$

$$\langle p_T^2 \rangle = 0.206 \pm 0.068 \ (\text{GeV/c})^2 \quad \text{for } 0.20 \leq x \leq 0.45$$

(*) The effect of using a $(1 + \cos^2\theta)$ distribution rather than an isotropic distribution would be to slightly steepen the x and p_T^2 distributions while increasing the acceptance-corrected cross section by ~7%.

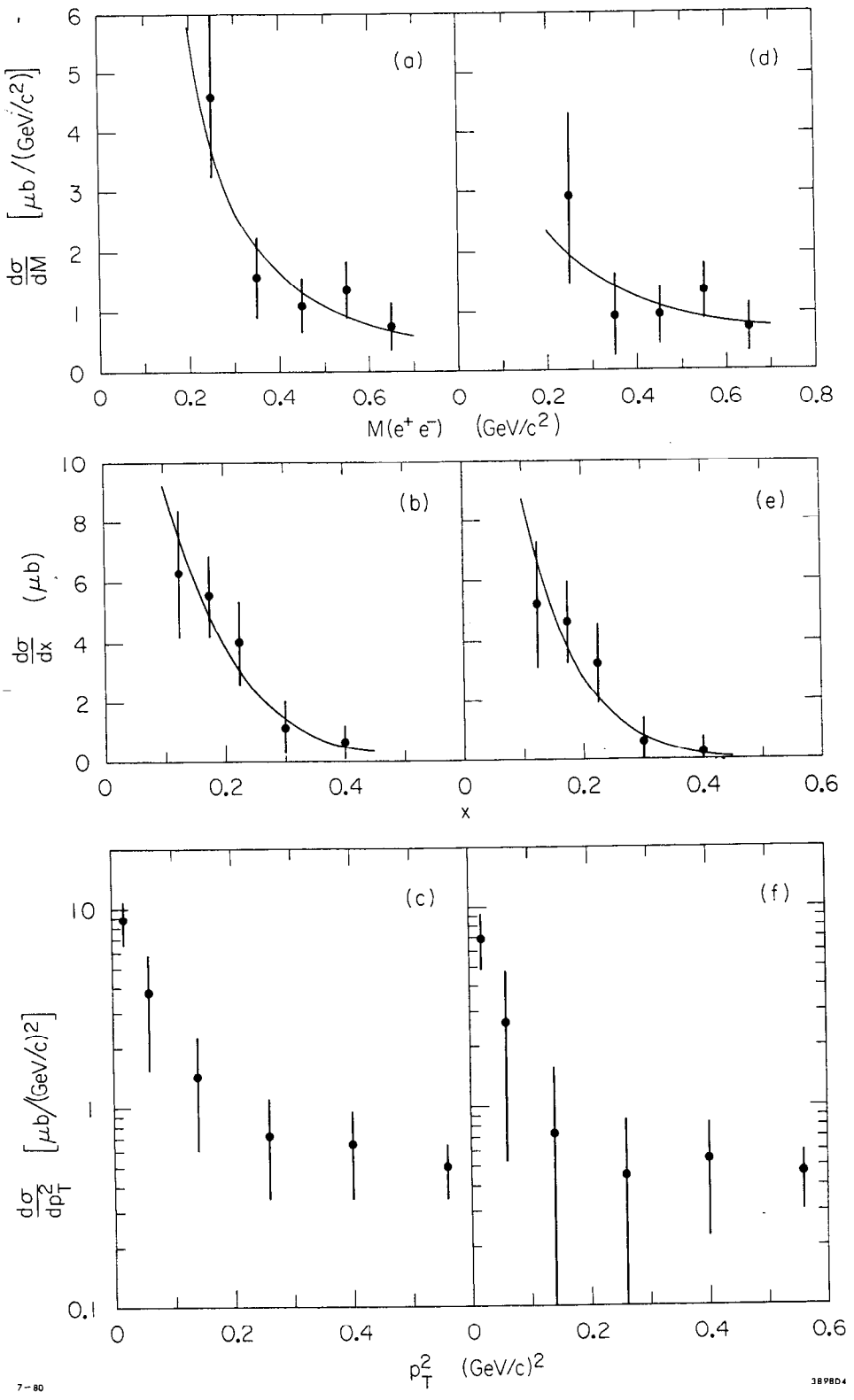

Fig. 13. The acceptance corrected mass, x and p_T^2 distributions for the continuum: (a)-(c) before, (d)-(f) after subtraction of the η and ω Dalitz decay contributions. The curves correspond to the fits described in the text.

indicating that the p_T^2 distribution may exhibit some x dependence. Indeed, the p_T^2 distributions for $x \leq 0.20$ and $x \geq 0.20$ (not shown) exhibit a significant growth of the low p_T^2 spike with decreasing x. This indicates that the effect is not associated with η and ω contributions (cf. Fig. 12(c)).

For these reasons, no attempt has been made to parametrize the distributions of Figs. 13(c) and (f).

3.5 The $(e^+e^-/\pi^+\pi^-)$ Ratio

The acceptance corrected e^+e^- cross sections obtained as described in the previous section may now be compared to the corresponding $\pi^+\pi^-$ pair data. Again the π^-p bubble chamber data [17] have been used for this study: $\pi^+\pi^-$ pairs have been selected which satisfy

$$0.10 \leq x \leq 0.45$$

$$0.0 \leq p_T^2 \leq 0.64 \ (\mathrm{GeV/c})^2$$

$$M(\pi^+\pi^-) \leq 0.7 \ \mathrm{GeV/c}^2 \ ,$$

and the $e^+e^-/\pi^+\pi^-$ cross section ratio was calculated as a function of M, x and p_T^2. For this purpose the η and ω contributions to the e^+e^- cross section have not been subtracted since the corresponding subtraction cannot be performed for $\pi^+\pi^-$ pairs. The overall $(e^+e^-/\pi^+\pi^-)$ ratio for the acceptance region defined above is $(6.4 \pm 1.2) \times 10^{-5}$; the effect of subtracting the (η, ω) contribution to the numerator is to reduce the ratio to $(4.7 \pm 1.2) \times 10^{-5}$.

The results scaled by the factor 10^5 are shown in Fig. 14. In Fig. 14(a) the bin $0.2 \leq M \leq 0.3$ GeV/c^2 has been excluded because of the

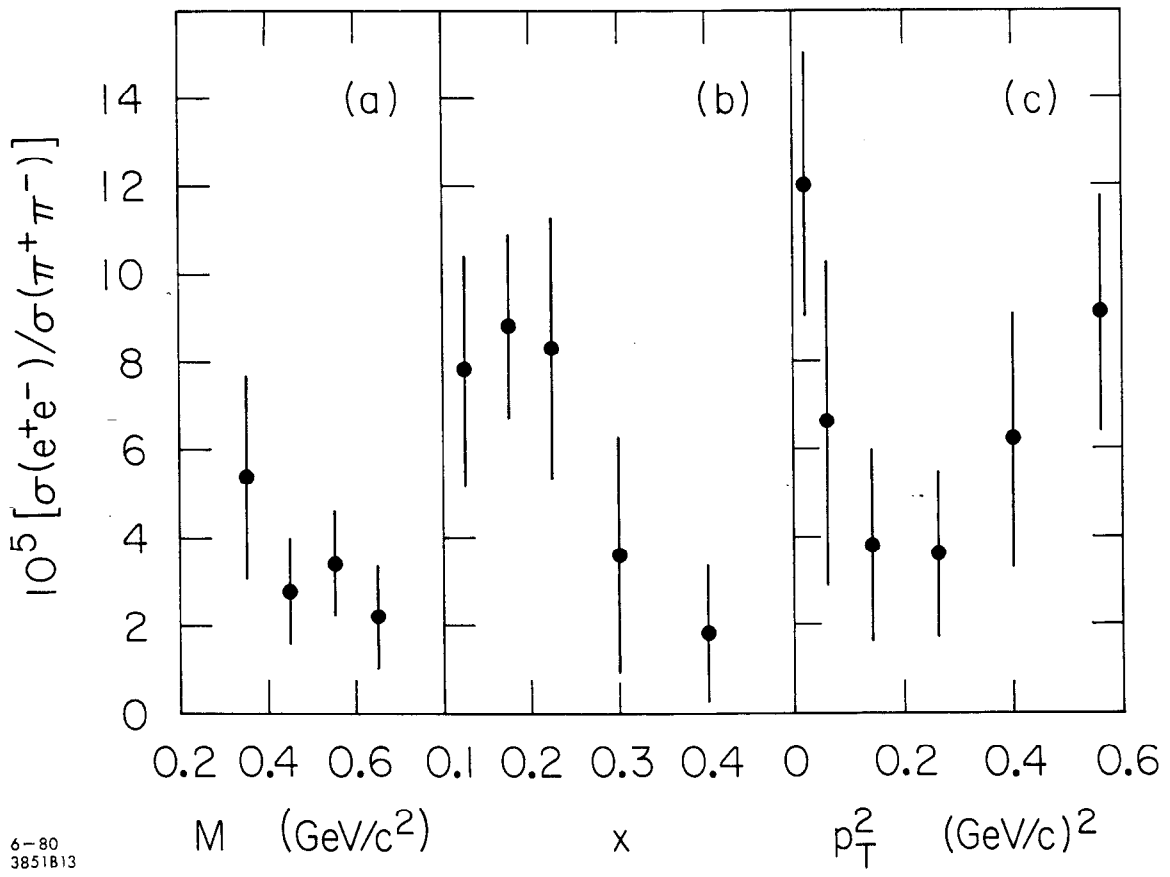

Fig. 14. The ratio of the cross section for e^+e^- and $\pi^+\pi^-$ production as a function of mass, x and p_T^2 for the region of phase space accessible to the present experiment.

two pion mass threshold. However, the events from this bin are included in Figs. 14(b) and (c).

Figure 14 indicates that the $(e^+e^-/\pi^+\pi^-)$ ratio exhibits strong x and p_T^2 dependence, which is not significantly changed when the events in the range $0.2 \leq M \leq 0.3$ GeV/c^2 are removed; however, its dependence on mass appears rather weak.

Subtraction of the η and ω contributions to the e^+e^- cross section produces no qualitative change in Figs. 14(b) and (c). However, Fig. 14(a) exhibits even less mass dependence, and the data in the range $0.3 \leq M \leq 0.7$ GeV/c^2 yield an average value for the $(e^+e^-/\pi^+\pi^-)$ ratio of $(2.7 \pm 0.9) \times 10^{-5}$.

3.6 Direct Photon Production

The production of direct e^+e^- pairs via the emission of a virtual photon as illustrated in Fig. 15(a) implies [21] the emission of direct photons by the same reaction mechanism. These processes may be related by [22]

$$\left[\frac{d^3\sigma_{e^+e^-}}{dMdxdp_T^2}\right] = \frac{2\alpha}{3\pi}\left(1 + \frac{2\mu^2}{M^2}\right)\sqrt{1 - \frac{4\mu^2}{M^2}}\ \frac{1}{M}\frac{|\vec{p}^*|}{E^*}\frac{f(M,x,p_T^2)}{f(0,x,p_T^2)}\left[\frac{d^2\sigma_\gamma}{dxdp_T^2}\right] .$$

Here μ is the electron mass, $\vec{p}^*$ and E^* are the c.m. momentum and energy of the pair, and $f(M, x, p_T^2)$ is the structure function for production of a virtual photon of mass M summed over photon polarization states.

The mass distribution of the direct pair events weighted by the factor

$$\frac{3\pi}{2\alpha}\frac{ME^*}{|\vec{p}^*|}\left(1 + \frac{2\mu^2}{M^2}\right)^{-1}\left(1 - \frac{4\mu^2}{M^2}\right)^{-0.5} \qquad (1)$$

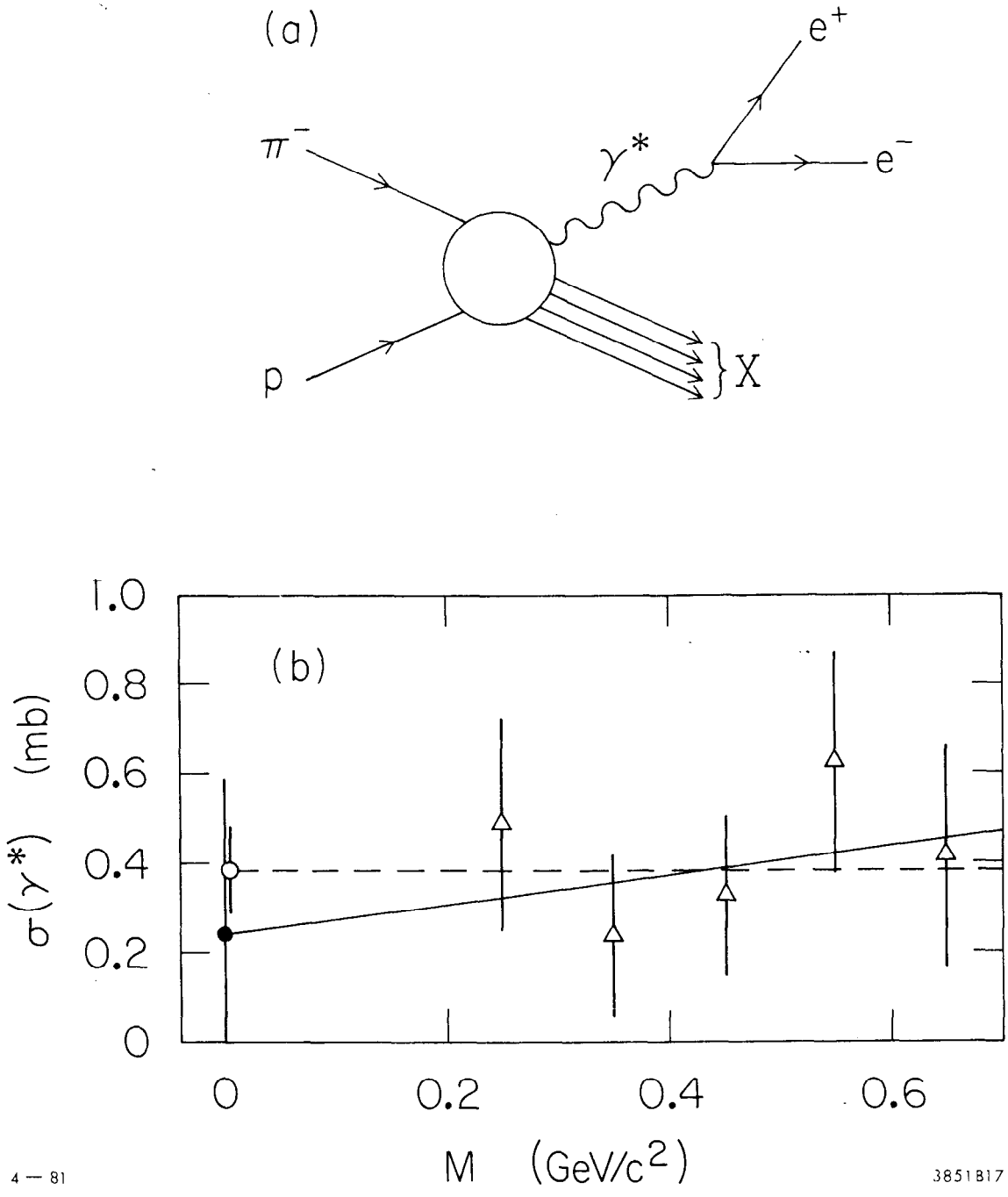

Fig. 15. (a) A schematic representation of the inclusive production of direct e^+e^- pairs via the emission of a virtual photon; (b) the mass dependence of the extrapolation function, $\sigma(\gamma^*)$, for direct photon production as described in the text. The direct e^+e^- events have been weighted according to (1) and the corresponding weighted contributions from η and ω Dalitz decays subtracted. The dashed line corresponds to an M-independent extrapolation function, the solid line results from the assumption of a linear M-dependence.

constitutes a measure of

$$\frac{f(M,x,p_T^2)}{f(0,x,p_T^2)}\left[\frac{d^2\sigma_\gamma}{dxdp_T^2}\right] \qquad (2)$$

integrated over the region of acceptance, i.e., in this experiment

$$0.10 \leq x \leq 0.45 \text{ and } 0 \leq p_T \leq 0.8 \text{ (GeV/c)} \quad .$$

This cross section, denoted by $\sigma(\gamma^*)$, is plotted in Fig. 15(b) as a function of M. In obtaining the data points of Fig. 15(b) the η and ω contributions weighted according to (1) have been subtracted since they would yield contributions corresponding to $\eta \to 2\gamma$ and $\omega \to \gamma\pi^o$ at the photon pole.

The error bars in Fig. 15(b) clearly preclude any significant conclusion as to the mass dependence of (2). However the extrapolation to the pole has been performed under two particular assumptions:

(i) expression (2) is independent of M; this yields a cross section estimate of (386 ± 95) μb for direct photon production;

(ii) expression (2) depends linearly(*) on M; this yields a direct photon production cross section estimate of (240 ± 350) μb.

In order to estimate the direct γ to π^o production ratio, the above direct γ cross section values were compared to those for inclusive π^+ production in π^-p interactions [17] in the same range of x and p_T^2.

(*) Any longitudinal polarization of the virtual photon yields a contribution to $\sigma(\gamma^*)$ which vanishes at the photon pole. This would imply a possible mass-dependence of the structure function.

The values obtained for (γ/π) are $(5.1 \pm 1.3)\%$ and $(3.2 \pm 4.7)\%$ for estimates (i) and (ii) of the direct photon cross section.

4. Comparison with Other Experiments

4.1 Electron Pair Production

Almost all previous experiments measuring the e^+e^- mass spectrum in the region below 0.7 GeV/c^2 suffer greatly from lack of statistics. This results in some confusion as to the existence or non-existence of a direct e^+e^- continuum signal in excess of known resonance contributions.

In π^+p interactions at 4 GeV/c [10] and 18 GeV/c [9], and in π^-p interactions at 70 GeV/c [11] it is claimed that the observed continuum, which typically contains $\lesssim$12 events, is accounted for by η and ω Dalitz decays. Furthermore, in a low energy $\bar{p}p$ annihilation experiment [12], the continuum contains 11 events while the estimated (η, ω) contribution is 6 ± 4 events.

In contrast, the π^-p data of reference 9 exhibit a continuum containing 16 ± 5 events in excess of the estimated (η, ω) Dalitz decay spectrum. This signal is strongly localized to low p_T and low x, in agreement with the results of the present experiment.

In addition to these bubble chamber experiments, there exist data for $x \sim 0$ and high p_T from two experiments at the ISR. The first [8] shows ~18 pairs with an estimated ~9 (η, ω) Dalitz decays for $0.2 \leq M(e^+e^-) \leq 0.5$ GeV/c^2 and $2 < p_T < 3$ GeV/c. The second experiment [7] exhibits a clear e^+e^- continuum containing ~150 events in the range $0.16 \leq M(e^+e^-) \leq 0.60$ GeV/c^2 for $p_T > 1.8$ GeV/c; (η, ω) Dalitz decays can account for the observed spectrum below ~0.25 GeV/c^2, but cannot account for the events in the range 0.4 - 0.6 GeV/c^2. These

events are described in terms of production and semi-leptonic decay of $D\bar{D}$ pairs, and this interpretation would again imply that the low mass continuum results from known sources.

In contrast to these experiments, the present experiment yields relatively good statistics in a regime where charmed particle production is negligible; the results presented in chapter 3 clearly demonstrate the existence of a low mass continuum which cannot be attributed to known sources.

There is another low energy spectrometer experiment to study e^+e^- pair production in π^-p interactions at 17 GeV/c for which analysis is still in progress. Preliminary results [23] with comparable statistics are quite consistent with those of the present experiment. The existence of a low mass continuum excess is again clearly established; however, detailed comparison with the present experiment must await final results from this MPS experiment.

4.2 Muon Pair Production at 16 GeV/c

In comparing dielectron and dimuon data, the assumption is made that the production mechanism in each case is as illustrated in Fig. 15(a) and that only effects associated with the lepton mass value need be taken into account. The lepton mass, μ, occurs explicitly only in the factor

$$F(\mu) = \left(1 + \frac{2\mu^2}{M^2}\right)\sqrt{1 - \frac{4\mu^2}{M^2}} \qquad (3)$$

describing the coupling of a virtual photon to a dilepton system of mass M. It follows that the comparison may then be effected by eliminating from the electron pair sample those pairs of mass below dimuon

threshold, and assigning to each remaining pair weight $F(m_\mu)/F(m_e)$, with F given by (3).(*)

The experiment measuring dimuon production in $\pi^{\pm}p$ interactions at 15.5 GeV/c [6] has good acceptance down to dimuon threshold in the region $x \geq 0.3$ and $p_T \lesssim 1.2$ GeV/c, and is thus complementary in x to the present experiment. The composite x distribution for $x \geq 0.1$ and $M \leq 0.6$ GeV/c^2 is shown in Fig. 16(a). The weighted electron data [24] match quite smoothly to the muon data, and the resulting total cross section for $x \geq 0.1$ is 864 ± 124 nb.

The shaded band of Fig. 16(a) represents the estimated contributions from direct ρ-decay and (η, ω) Dalitz decay; its width reflects the uncertainty in the values of the relevent inclusive cross sections. It is apparent that the fraction of the low mass continuum which is not attributable to known sources increases rapidly with decreasing x. The subtracted spectrum of Fig. 16(b) is well described by a single exponential function of the form

$$\frac{d\sigma}{dx} = Ae^{-bx}$$

with slope $b = 6.3 \pm 0.1$; a function of the form

$$\frac{d\sigma}{dx} = C(1 - x)^{\beta}$$

with $\beta \sim 4.2$ describes the region $x \leq 0.8$ reasonably well, but falls off too rapidly at larger x. For the e^+e^- data alone $\beta = 9.8 \pm 2.6$ was

---

(*) This procedure reduces the e^+e^- cross section for $0.2 \leq M \leq 0.7$ GeV/c^2 by about one third.

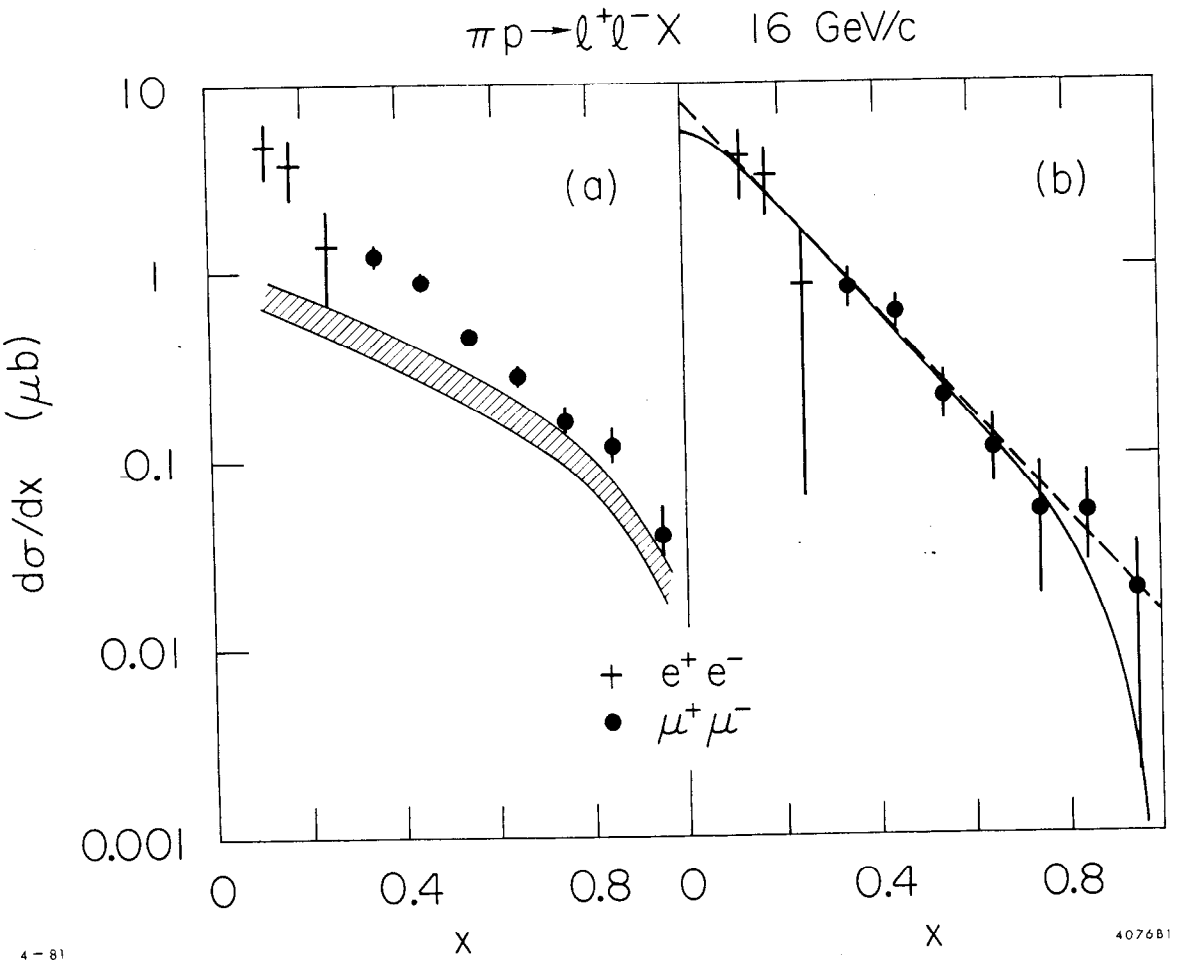

Fig. 16. (a) The composite dilepton x distribution at 16 GeV/c for $M \leq 0.6$ GeV/c^2; the shaded band represents the estimated contribution from direct ρ-decay and (η, ω) Dalitz decay; (b) the subtracted spectrum corresponding to Fig. 16(a); the dashed line is an exponential of slope 6.3, and the curve results from the calculation described in the text.

obtained (Section 3.4); the change results from the good precision of the muon data together with the extended x range of the fit.

The residual cross section corresponding to Fig. 16(b) is 608 ± 135 nb [25], so that only ~30% of the continuum cross section for $M \leq 0.6$ GeV/c^2 and $x \geq 0.1$ can be attributed to known sources.

The composite p_T^2 distribution and the estimated contribution from known resonances are shown in Fig. 17(a) for $M \leq 0.6$ GeV/c^2. Their difference is shown in Fig. 17(b); also shown are the distributions corresponding to the continuum excess for $x \geq 0.3$ (Fig. 17(b)) and $0.1 \leq x \leq 0.3$ (Fig. 17(c)). The curves result from the calculation to be discussed in section 5.3 below.

The distributions shown in Fig. 17 exhibit an x dependence which is very similar to that resulting from η and ω Dalitz decay except at low x and $p_T^2 \leq 0.04$ $(\text{GeV}/c)^2$ (cf. Fig. 17(c)). This is shown explicitly in Fig. 18, where the variation of $\langle p_T^2 \rangle$ with x is plotted; the data points correspond to the unsubtracted low mass continuum, whereas the dashed curve corresponds to the estimated η and ω Dalitz decay contributions. The curve describes the data quite well despite the decrease of the Dalitz contribution from ~50% for $x \geq 0.8$ to ~15% for $x \sim 0.1$.

The mass distributions corresponding to the continuum excess for the weighted e^+e^- data and the $\mu^+\mu^-$ data will be discussed in Section 4.3.

Since the weighted electron data match well to the dimuon data, the combined data sample will be considered equivalent to that for a dimuon experiment of extended acceptance. In subsequent discussion, references to this combined sample will be denoted by the use of an italicized *dimuon*.

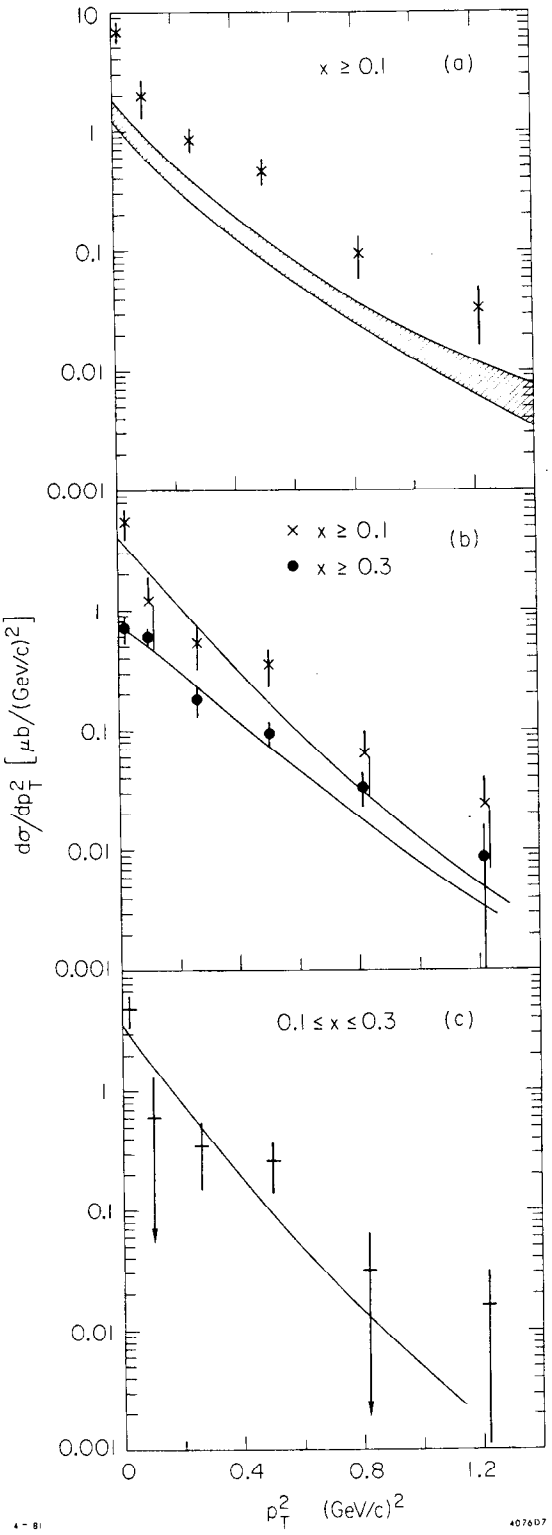

Fig. 17. (a) The composite dilepton p_T^2 distribution at 16 GeV/c for $M < 0.6$ GeV/c^2; the shaded band represents the contribution from known resonances; (b) the subtracted spectra corresponding to Fig. 17(a) for $x \geq 0.1$ and $x \geq 0.3$; (c) the subtracted spectrum for $0.1 \leq x \leq 0.3$; the curves displayed in (b) and (c) result from the calculations described in the text.

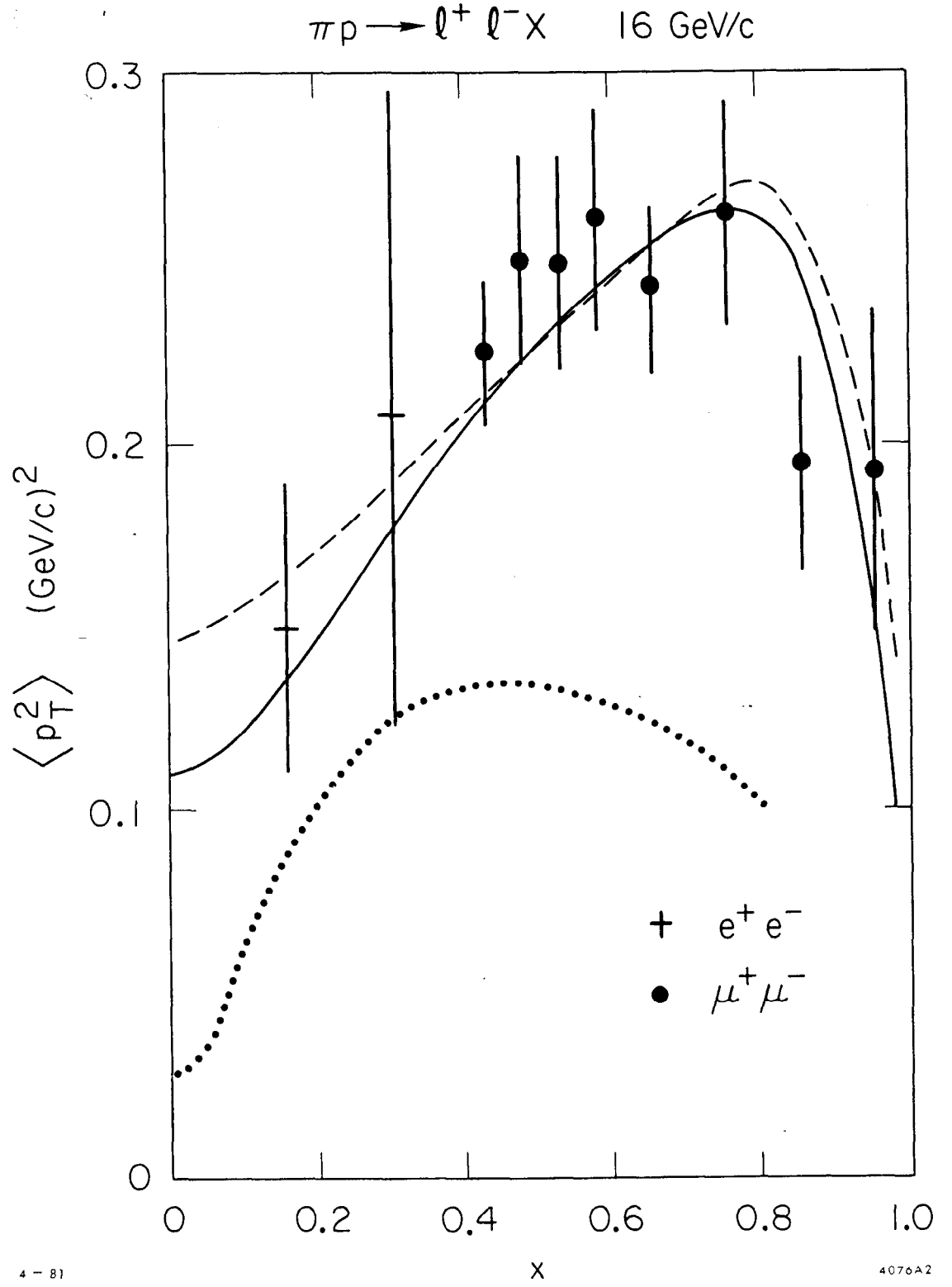

Fig. 18. The variation of $\langle p_T^2 \rangle$ with x for the composite dilepton data at 16 GeV/c in the range $M \leq 0.6$ GeV/c^2; the dashed curve represents the corresponding variation for the estimated η and ω Dalitz decay contributions, and the dotted curve that for electron pairs from π^0 Dalitz decay; the solid curve results from the calculation described in the text.

4.3 Muon Pair Production at 225 GeV/c

In order to investigate the energy dependence of the anomalous low mass signal, relevant data on dimuon production in π^-C interactions at 225 GeV/c [26-30] are now compared in some detail with the 16 GeV/c results. In this context, it is assumed that the x dependence of ρ, ω and η production is given by the dimuon data in the range $0.65 \leq M \leq 0.93$ GeV/c^2 [26]. Similarly, it is assumed that the p_T^2 distribution for ω production may be obtained from this interval. An exponential p_T^2 dependence with slope value of ~ 2.5 $(\text{GeV/c})^{-2}$ is indicated, and it is further assumed that this behaviour also describes η production (cf., 16 GeV/c). Lastly, the relative production rates for ρ, ω and η are taken to be the same as at 16 GeV/c.

The x and p_T^2 distributions for the 225 GeV/c π^-C data in the region $x \geq 0.07$ and $M \leq 0.65$ GeV/c^2 are shown in Figs. 19(a) and (c) respectively;(*) the data of reference 26 have been converted to cross section/nucleon by means of the factor $A^{-\alpha}$ with $\alpha = 0.65 \pm 0.05$ [27].

The estimated contributions from known sources are shown as shaded bands in Figs. 19(a) and (c), and the corresponding subtracted distributions are presented in Figs. 19(b) and (d) respectively; the distribution of Fig. 19(d) has been normalized (scale factor 0.66) to the 16 GeV/c *dimuon* data in the region $x \geq 0.1$, $M \leq 0.6$ GeV/c^2 in order to make a direct shape comparison.

(*) Although discussion is confined to the π^-C data of reference 26, it should be noted that the low mass distributions in x, p_T^2 and M for π^+C and π^-C are virtually identical.

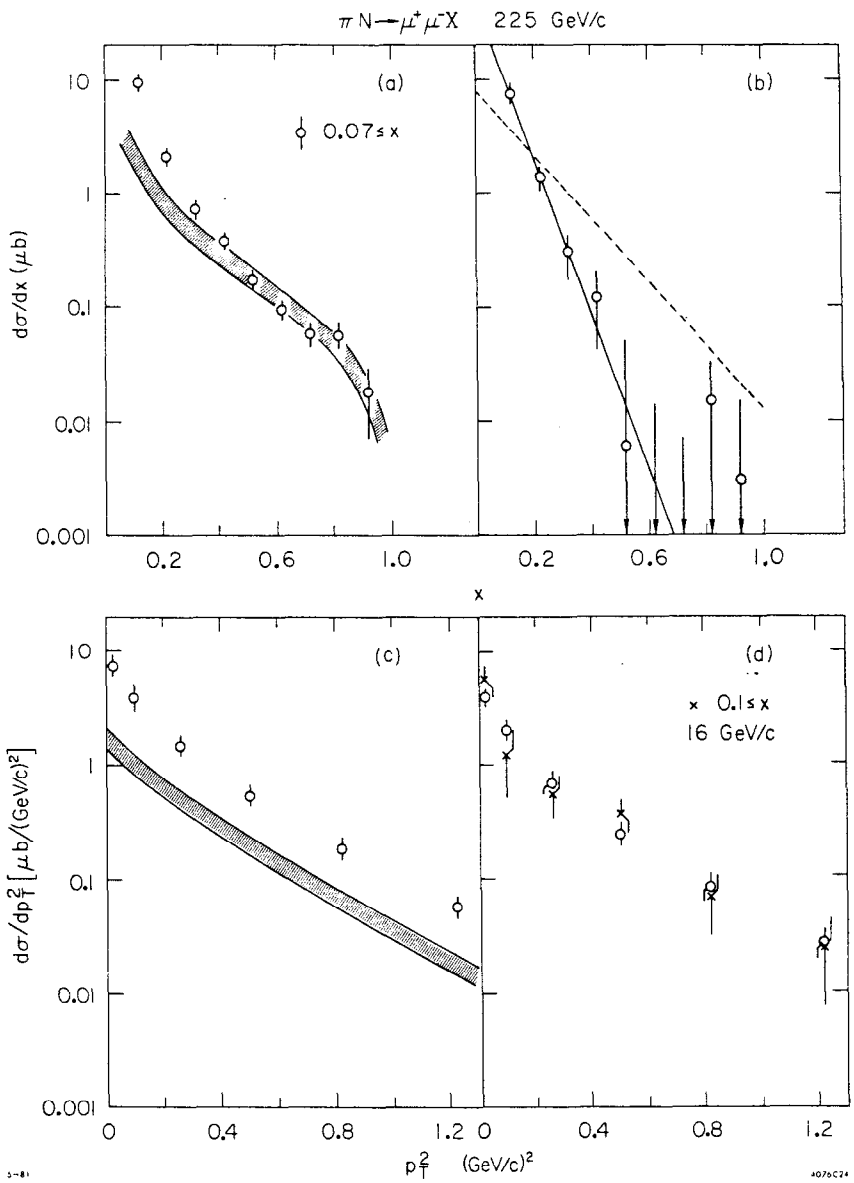

Fig. 19. The x and p_T^2 distributions for $\pi N \to \mu^+\mu^- X$ in the region $x \geq 0.07$, $M \leq 0.65$ GeV/c^2 resulting from π^-C interactions at 225 GeV/c; the shaded bands in (a) and (c) represent the estimated contributions from η and ω Dalitz decay as well as direct ρ and ω decay; the subtracted distribution of (b) is described by a single exponential of slope 15.9 (solid line); the corresponding fit to the 16 GeV/c data (dashed line) is also shown; the subtracted distribution in (d) has been normalized (scale factor = 0.66) to the corresponding distribution for $x \geq 0.1$, $M \leq 0.6$ GeV/c^2 at 16 GeV/c, which is shown for comparison.

From Figs. 19(a) and (b), it appears that essentially all of the low mass continuum for $x \geq 0.5$ results from known sources, and that the x distribution for the anomalous signal is much steeper at 225 GeV/c than at 16 GeV/c. The solid line of Fig. 19(b) is an exponential of slope 15.9, and describes the 225 GeV/c data quite well; the dashed line, of slope 6.3, is the result of the previously-described fit to the 16 GeV/c data. The fact that these lines exhibit a pronounced cross-over indicates that the structure function describing the anomalous continuum does not scale between 16 and 225 GeV/c.

The continuum cross section at 225 GeV/c for $x \geq 0.07$ and $M \leq 0.65$ GeV/c^2 is 1279 ± 173 nb; after subtracting the estimated contributions from known sources the residual cross section corresponding to the anomalous continuum in this region is 916 ± 190 nb.

The p_T^2 distribution for the continuum excess [Fig. 19(d)] has essentially the same shape as that obtained for known sources [Fig. 19(c)] for $p_T^2 \geq 0.2$ (GeV/c)^2; at lower p_T^2 values, however the anomalous distribution is steeper. The overall shape agrees quite well with that obtained at 16 GeV/c [Fig. 19(d)], however, the x - p_T^2 correlation is somewhat different [28].(*)

In Fig. 20(a), the dimuon mass distribution at 225 GeV/c for $x \geq 0.07$ is shown in conjunction with the estimated contribution from known sources. The subtracted distribution, normalized to the 16 GeV/c *dimuon* data for $x \geq 0.1$, is compared in Fig. 20(b) with the 16 GeV/c data. There is reasonable shape agreement within the rather large

---

(*) $\langle p_T^2 \rangle$ increases from ~0.2 (GeV/c)^2 at x = 0.1 to ~0.35 (GeV/c)^2 at x = 0.4.

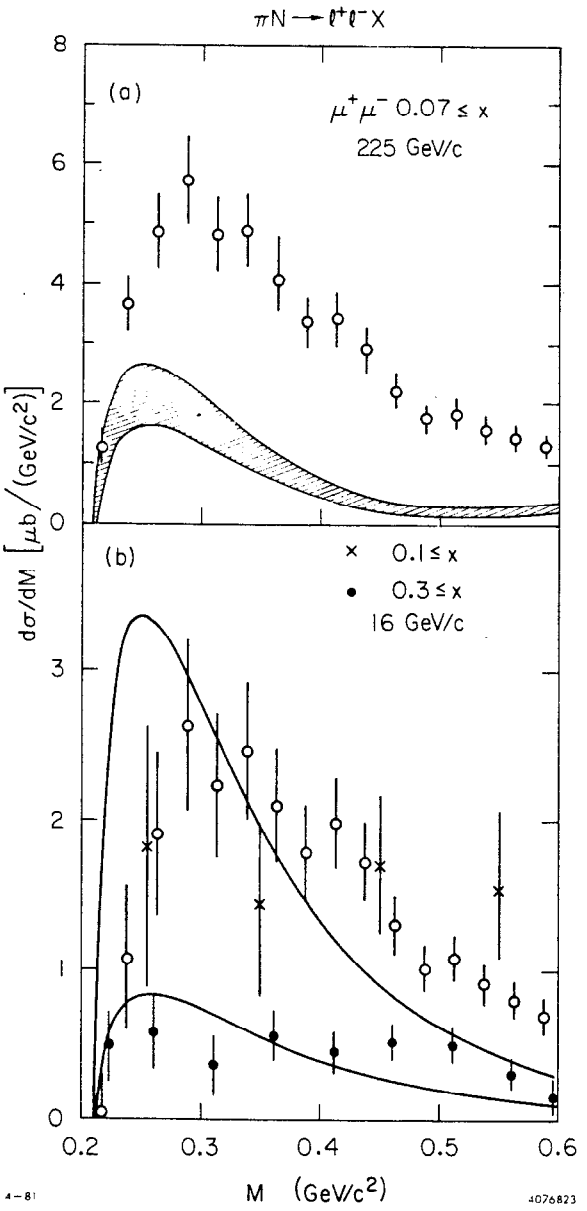

Fig. 20. (a) The dimuon mass distribution for $\pi N \to \mu^+\mu^- X$ for $x \geq 0.07$ resulting from π^-C interactions at 225 GeV/c; the shaded band represents the estimated contributions from η and ω Dalitz decay as well as direct ρ and ω decay; (b) the subtracted distribution resulting from (a) normalized (scale factor = 0.684) to the 16 GeV/c data for $x \geq 0.1$; the corresponding 16 GeV/c distribution and that for dimuons at 16 GeV/c are also shown; the curves result from the calculation described in the text.

uncertainties of the low energy data. In contrast the 16 GeV/c dimuon distribution ($x \geq 0.3$) is much broader than that at 225 GeV/c ($x \geq 0.07$), suggesting the existence of a significant (M, x) correlation. Indeed fits to the x distribution for $M \leq 0.45$ GeV/c^2 and $0.45 \leq M \leq 0.65$ GeV/c^2 in πC interactions at 225 GeV/c [26] and p Be interactions at 150 GeV/c [29] indicate that the x distribution of the low mass continuum is decreasing in steepness with increasing mass.

The large uncertainties associated with the weighted e^+e^- data at 16 GeV/c allow no conclusion to be drawn concerning the existence of such an (M, x) correlation.

5. Possible Sources of the Anomalous Dilepton Continuum

5.1 Models

As discussed in Section 4.1, the authors of reference 7 attribute a sizeable fraction of the low mass continuum to the production and semi-leptonic decay of charmed particle pairs. A similar interpretation of the 16 GeV/c data would result in charmed particle cross section values in the range 0.1 - 1 mb. Actual values are estimated to be $\leq$10 μb and so charmed particle production must be ruled out as a significant source of the anomalous continuum.

The Drell-Yan mechanism [2] describes dilepton production in terms of the annihilation of valence quarks in the initial state particles in an impulse approximation approach. As such it is expected to be valid at high dilepton mass, but not in the region of the low mass continuum. This appears to be the case; for example, in reference 30 it is shown that the high mass ($\geq$4 GeV/c^2) description when extrapolated to low mass falls below the observed dimuon spectrum at $M = 0.6$ GeV/c^2 by a factor of $\sim$15.

Bjorken and Weisberg [31] suggested that the low mass continuum might result primarily from the annihilation of centrally-produced $q-\bar{q}$ pairs. This idea was made quantitative by Cerny et al. [32], who in addition incorporated the concept of space-time evolution of the collision in order to localize the effect to low mass. The resulting mass distribution agreed fairly well with the data, but the corresponding x and p_T^2 spectra were not very well reproduced. A subsequent modification to this model [33] will be discussed in the next section.

A second class of models is based on the idea of internal conversion of virtual photons generated by the bremsstrahlung of virtual charged particles produced in the interaction [34]. This mechanism will also be considered in more detail in the next section.

Other models, such as those based on thermodynamical concepts [35] and those formulated in terms of pion-pion and quark-pion interactions [36] will not be considered here.

5.2 An Empirical Approach

As discussed previously, the principal features of the anomalous continuum are the steepness of the x distribution and the development of a sharp, low p_T^2 peak as x decreases from $\sim$0.25 toward zero.

These characteristics essentially preclude the possibility that the dilepton continuum results predominantly from a high mass source. Resonances above the ρ are known to have much flatter x and p_T^2 distributions than those observed for the low mass continuum. Furthermore, if the dilepton system results from the decay of such a high mass object, the sharpening of the p_T^2 distribution due to parent-daughter kinematics does not yield a very steep low p_T^2 peak.

In Fig. 21 it is shown that the composite x distribution for the anomalous continuum at 16 GeV/c is very similar in shape to that for dielectrons from the Dalitz decay of π^o's produced in πp interactions at 18 GeV/c [37]. The p_T^2 distribution for such dielectrons develops a very steep low p_T^2 peak for $x \leq 0.3$, as illustrated by the dotted curve of Fig. 18. This behaviour is qualitatively similar to that observed for the dilepton continuum at low x although, as discussed previously, the behaviour for $x \geq 0.3$ more closely resembles that for η and ω Dalitz decay.

On the basis of these observations, the conjecture is made that the anomalous dilepton continuum results from a broad parent(*) continuum distribution reaching a maximum in the vicinity of the η and ω, but extending in significant strength to low mass and also, presumably, exhibiting a high mass tail. The parent x distribution should resemble that for the pion (although there may be significant mass-x correlations), and the decay mechanism resulting in the dilepton continuum should be essentially Dalitz-like. In order to relate such a conjecture to the models discussed in the previous section, these ideas are now re-expressed in terms of quarks.

The Drell-Yan mechanism, illustrated by Fig. 22(a), involves an initial $q\text{-}\bar{q}$ system in a state with quantum numbers $J^{PC} = 1^{--}$, with spin S = 1 and orbital angular momentum predominantly L = 0. As discussed

---

(*) It should be noted that the dashed curve of Fig. 18 is obtained from parent η and ω distributions for which $\langle p_T^2 \rangle = 0.345$ (GeV/c)^2 at all x.

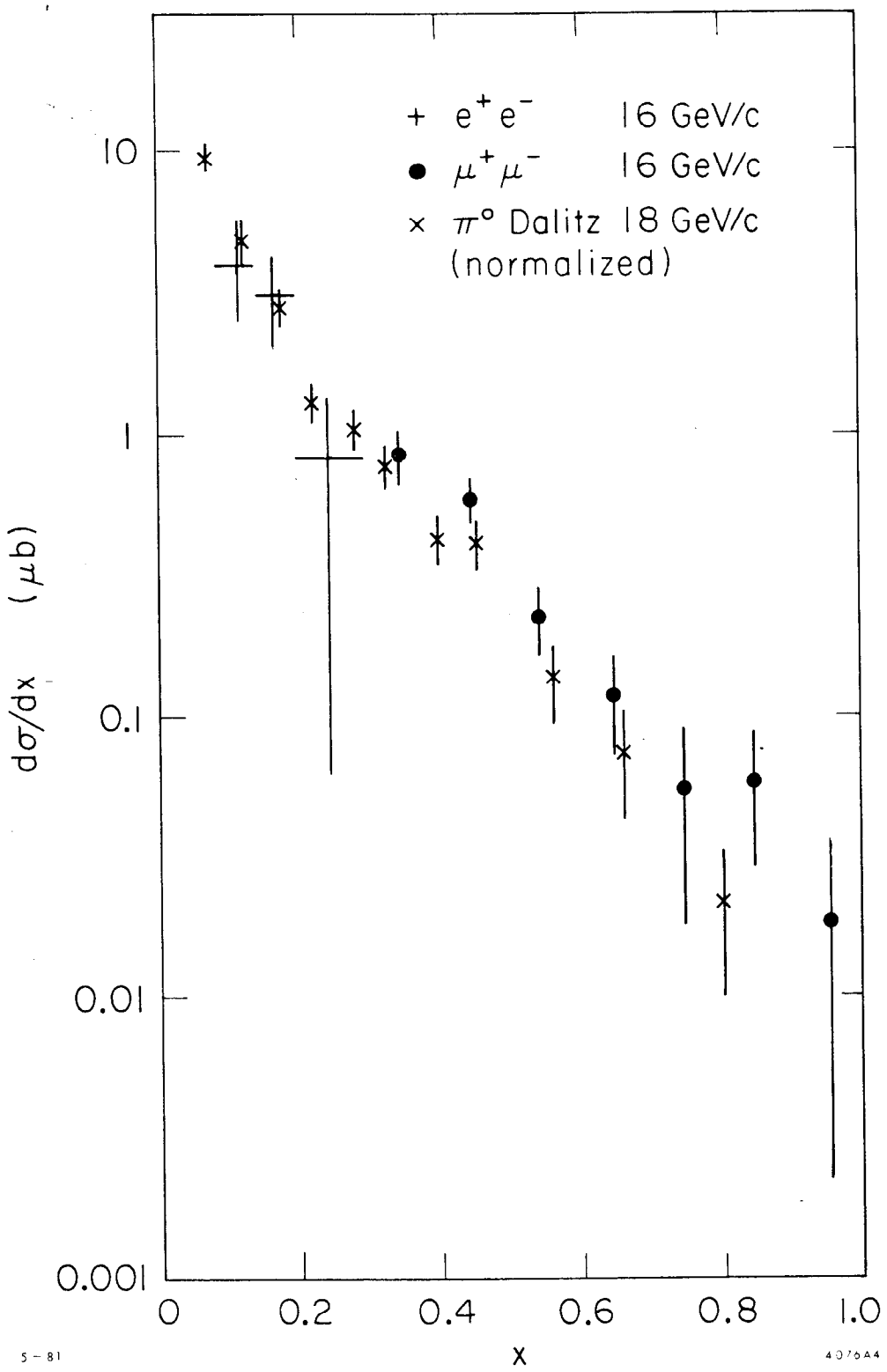

Fig. 21. The composite x distribution for the anomalous continuum at 16 GeV/c in comparison with that for dielectrons resulting from the Dalitz decay of π^o's produced in πp interactions at 18 GeV/c; the π^o data have been normalized to the 16 GeV/c data for $0.10 \leq x \leq 0.25$.

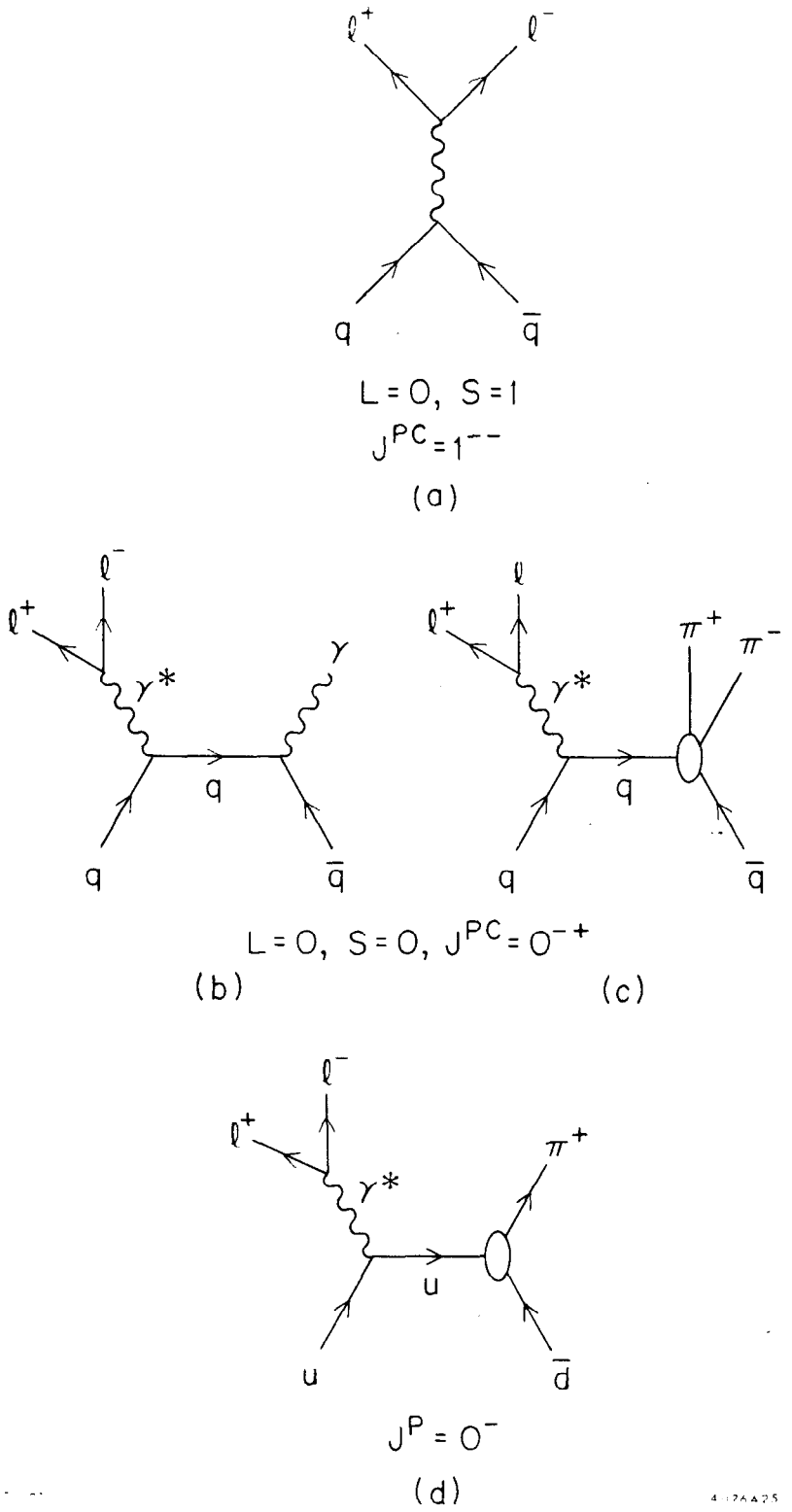

Fig. 22. Diagrams illustrating the dilepton production mechanisms discussed in the text: a) Drell-Yan, b) generalized Dalitz decay, c) $q\bar{q}$ annihilation to a virtual photon and a dipion system with the ρ^o quantum numbers, d) inner bremsstrahlung.

in Section 5.1, this mechanism seems to be of little relevance to a description of low mass dilepton production.

If in the lowest orbital angular momentum state the quark spins couple to S = 0, the resulting quantum numbers are $J^{PC} = 0^{-+}$, and the lowest mass hadronic system to which such a $q\bar{q}$ system can couple (other than the pion itself) contains three pions. It follows that such a system will decay electromagnetically for masses ≤ 4.0 GeV/c^2 and would presumably continue to have significant electromagnetic coupling at higher mass. Figure 22(b) illustrates the corresponding Dalitz decay mechanism, and in Fig. 22(c) the on-shell photon has been replaced by the lowest mass allowed hadronic system(*) viz. $\pi^+\pi^-$ with the quantum numbers of the ρ. Since the $\pi^+\pi^-$ P-wave interaction at low mass is dominated by ρ it might be expected that the mechanism of Fig. 22(c) would be associated with $q\bar{q}$ systems of mass ≥ 1 GeV/c^2, taking into account the dilepton threshold. As will be shown below, such a high mass parent $q\bar{q}$ system does not yield a sufficiently steep p_T^2 distribution for the daughter dilepton system; for this reason it is conjectured that the Dalitz mechanism of Fig. 22(b) is the dominant $q\bar{q}$ annihilation source of low mass dilepton pairs.

The empirical approach outlined above thus leads to a conjecture which is very similar to the model proposed independently in references 31 and 32. The authors of reference 32 were led to propose a modification to their calculations in order to better describe the p_T dependence of the data. This modification [33] involves a Dalitz-like mechanism as

---

(*) Final states of the type $\gamma^* + n(\pi^o)$ with $n \geq 1$ are forbidden by C invariance.

in Fig. 22(b), but with the on-shell photon replaced by a gluon(*) so that it is more akin to the process of Fig. 22(c).

If $q\bar{q}$ pairs having the quantum numbers of the pion are indeed the source of the low mass continuum, then in addition to the annihilation mechanism of Fig. 22(b) there may also be a contribution when the quarks have different flavor. A simple mechanism by which this might occur is illustrated in Fig. 22(d), and may be considered to be an inner bremsstrahlung process of the type proposed in reference 34.

For parent masses above 0.2 GeV/c^2, the processes of Fig. 22(b) and (d) result in virtually indistinguishable x, p_T^2 and M distributions of the dilepton system.

However, the internal angular distribution of the lepton pair should be quite different in the two cases, since the annihilation process yields transversely polarized virtual photons ($m = \pm 1$) whereas the inner bremsstrahlung process results in longitudinal polarization ($m = 0$). In this regard, the general form of the angular distribution integrated over azimuth is [39]

$$W(\theta) = \frac{3\left\{1 - \left(1 - \frac{4\mu^2}{M^2}\right)\left(\rho^{00}\cos^2\theta + \rho^{11}\sin^2\theta\right)\right\}}{4\left(1 + \frac{2\mu^2}{M^2}\right)} \qquad (4)$$

where μ is the lepton mass and θ the helicity angle with respect to the dilepton line of flight; ρ^{00} and ρ^{11} are density matrix elements for the virtual photon. The angular distribution for $m = \pm 1$ corresponds to

---

(*) The Dalitz decay conjecture resulting from the empirical approach to the data was made prior to any knowledge of reference 33.

$\rho^{11} = 0.5$, $\rho^{00} = 0$ and at high mass this yields a $(1 + \cos^2\theta)$ dependence; m = 0 corresponds to $\rho^{11} = 0$, $\rho^{00} = 1$ with high mass angular distribution $\sim\sin^2\theta$.(*)

Unfortunately, the dielectron data of the present experiment are not sufficiently precise to yield useful information on the angular distribution. The dimuon distribution at 16 GeV/c for $M \leq 0.6$ GeV/c^2 [6] does tend to increase towards $\cos\theta = \pm 1$, but again the uncertainties are large.(**) There are no other data providing information on this question, and so it remains an important open issue which future experiments should address.

As mentioned previously the Drell-Yan mechanism appears to be the dominant source of high mass dileptons. The diagrams of Figs. 22(c) and (d) are of the same order in α (the e.m. coupling constant) as the Drell-Yan diagram so that some additional mechanism, such as the imposition of short-range order [32,33], is required to restrict their contribution to the low mass region. In contrast the Dalitz mechanism of Fig. 22(b) involves one additional power of α; consequently, at high mass where there is essentially a continuum of $J^P = 0^-$ and 1^- $q\bar{q}$ states, the Drell-Yan process should automatically dominate; at low mass, however, where the level structure is discrete and the 0^- states are lower-lying

---

(*) At threshold the angular distribution is isotropic in both cases; however, at $M = 6\mu$ the angular distributions are already $\sim 1 + 0.8\cos^2\theta$ and $\sim\sin^2\theta + 0.125$ for $m = \pm 1$ and $m = 0$ respectively.

(**) This distribution also contains contributions from η and ω Dalitz decay for which $m = \pm 1$, thereby increasing the uncertainty as to the continuum angular distribution.

than the corresponding 1^- states, it is not unreasonable that the Dalitz mechanism should be predominant.

5.3 Calculations for Dilepton Production at 16 GeV/c

In order to learn something of the general characteristics which should be required of parent $q\bar{q}$ systems of the type discussed in Section 5.2, the following initial procedure was followed at 16 GeV/c: the (x, p_T) distribution for the parent $q\bar{q}$ system of Fig. 22(b) was assumed to be that for inclusive π^+'s from π^-p interactions at 16 GeV/c [17]; every π^+ on the bubble chamber data tape was assigned the same parent mass value, and the Dalitz decay of this parent object generated [19]; distributions of interest for the secondary dimuon pairs were then accumulated.

The resulting distributions in x ($p_T \leq 1.2$ GeV/c) and p_T^2 ($0.1 \leq x \leq 0.3$) for dimuon pairs of mass less than 0.6 GeV/c^2 are shown in Fig. 23 as a function of parent mass in the range 0.4 - 1.5 GeV/c^2. It is clear that in order to obtain dimuon distributions exhibiting steep behaviour at low values of x and p_T^2, the parent mass spectrum should be strongly localized at masses $\leq$0.9 GeV/c^2. In addition, the dimuon mass spectrum resulting from the Dalitz decay matrix element [19] is essentially zero for masses $\geq$90% of the parent mass. Since the continuum mass spectrum of Fig. 20(b) appears to differ significantly from zero at 0.6 GeV/c^2 the implication is that there must be substantial contributions from parent mass values above 0.6 GeV/c^2.

The distributions of Fig. 23(a) show no broadening of the dimuon x distribution with increasing parent mass. It follows that in order to generate such a correlation for the dimuon pairs, the parent x

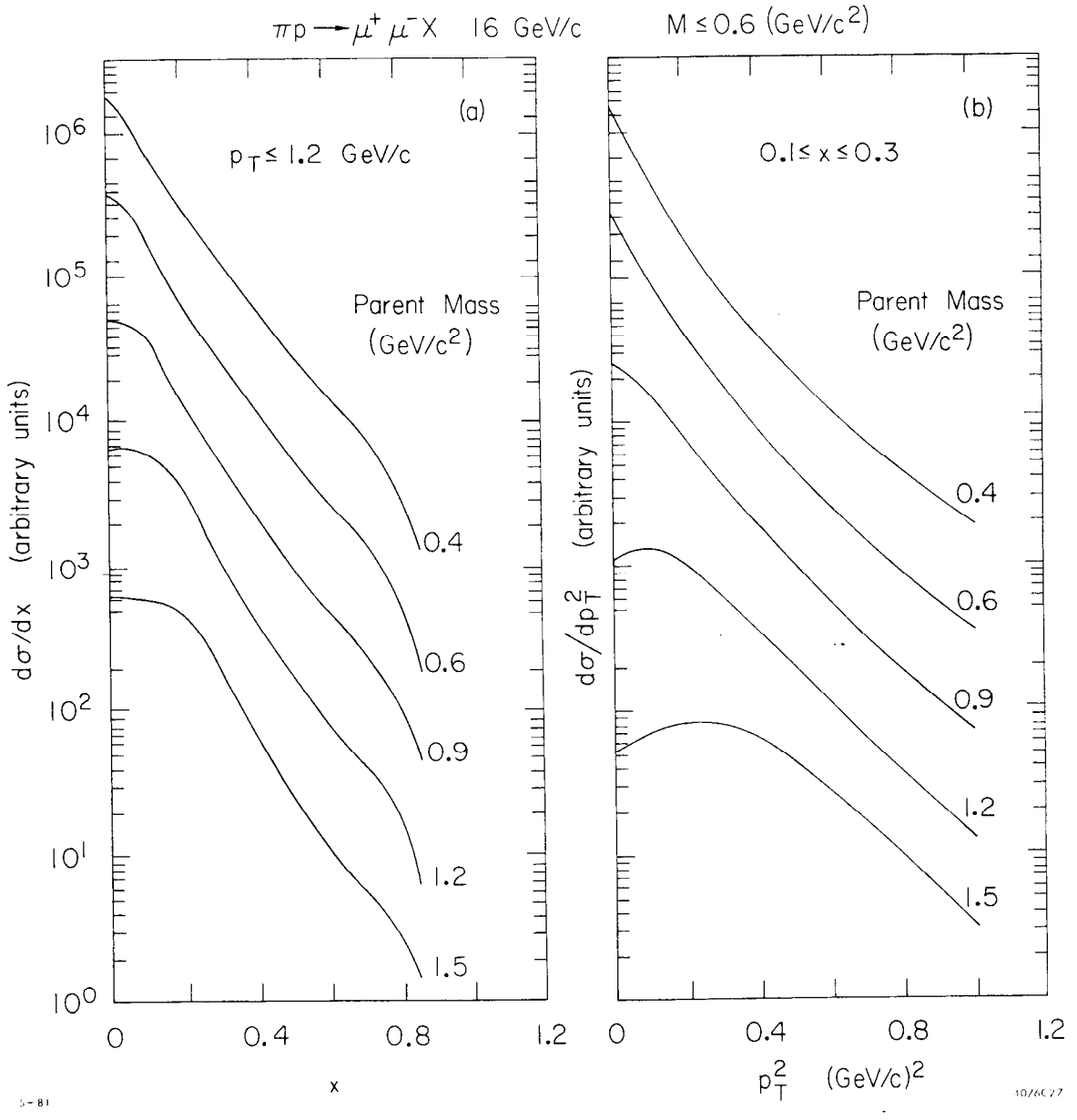

Fig. 23. The dependence of dimuon x and p_T^2 distributions on parent mass resulting from Dalitz decay of parent systems having the (x, p_T) distribution of inclusive π^+'s from πp interactions at 16 GeV/c.

distribution must be mass-dependent. A mass dependence is obtained using like charge pion pairs from the 16 GeV/c bubble chamber data tape [17]; the pions are assigned zero mass,(*) and the x distribution obtained for different intervals of $\pi\pi$ effective mass. For effective mass values in the vicinity of the pion mass, the x distribution is very similar to that observed for the pion. At higher masses, however, the distribution is observed to broaden, and the resulting mass-x correlation is represented to good approximation by

$$\frac{d\sigma}{dx} \sim e^{-bx}(1 - 0.5\ e^{-bx}) \tag{5}$$

with $b = 7.25 - 3.5\ M_p$ where M_p is the effective mass. The factor in parentheses yields the observed flattening of the $\pi\pi$ distributions for $x \sim 0$ but has little effect for $x \geq 0.2$.

The distribution of parent mass, M_p, obtained from the same sign pion pairs peaks at $M_p \sim 0.4$ GeV/c^2 and is skewed toward high mass. A similar mass distribution may be obtained by generating events according to

$$\frac{d\sigma}{dM_p} \sim \exp\left(-(M_p - 0.4)^2/2\sigma^2\right) \tag{6}$$

and then weighting events having $M_p \leq 0.4$ GeV/c^2 by $(M_p/0.4)$ in order to force the mass spectrum to zero at threshold. It is found empirically that the value $\sigma = 0.35$ GeV/c^2 yields a mass spectrum which is adequate for the present studies.

(*) The Dalitz matrix element yields the ratio of the Dalitz decay rate to the two-photon rate; it follows that the parent mass spectrum is a two-photon spectrum and it is for this reason that the pion is given the photon mass.

As discussed previously in the case of (η, ω) Dalitz decay, a parent p_T^2 distribution of constant slope yields a dimuon (x, $\langle p_T^2 \rangle$) correlation which is very similar to that observed at 16 GeV/c [cf. Fig. 18]. However, it is found that such a parametrization results in an average p_T for the dimuon system which decreases slightly with increasing mass. At 225 GeV/c [27], $\langle p_T \rangle$ has been observed to increase linearly with M. This indicates that it is necessary to introduce a parent p_T^2 distribution which depends on M_P. Using same sign pion pairs as before, the dependence of parent $\langle p_T^2 \rangle$ on x was studied as a function of parent mass. It was found that at low mass there exists a strong (x, $\langle p_T^2 \rangle$) correlation similar to that of Fig. 18, but that this correlation decreases markedly with increasing parent mass. Such behaviour can be obtained by generating a parent p_T^2 distribution according to

$$\frac{d\sigma}{dp_T{}^2} \sim \exp(-E/m_o) \tag{7}$$

where $E^2 = M_P^2 + (xp_i^*)^2 + p_T^2$; x is the parent x value and p_i^* is the incident momentum in the c.m. system. In the calculations an m_o value of 0.060 GeV/c^2 is used; the resulting description of the *dimuon* data for $p_T \leq 0.8 - 0.9$ GeV/c is found adequate, and $\langle p_T \rangle$ is found to increase approximately linearly with M. However at higher p_T values, (7) decreases too rapidly with increasing p_T, and any serious attempt at a description of dilepton data in this region requires a more elaborate representation than that embodied in (7).

The final procedure followed in attempting to describe the *dimuon* distributions at 16 GeV/c in terms of the Dalitz mechanism of Fig. 22(b) may then be summarized as follows:

(i) a 2γ parent mass distribution is generated according to (6) for $M_P \geq 0$, and a weight $(M_P/0.4)$ assigned each event having $M_P \leq 0.4$ GeV/c^2;

(ii) for each event an x value is generated according to (5) with x replaced by $|x|$ so that a symmetric x distribution will result;(*) subsequently a p_T^2 value is generated according to (7) using the relevant values of M_P and x;

(iii) the kinematic boundary is taken into account by discarding events for which the missing mass recoiling against the parent object is less than the neutron mass;

(iv) the Dalitz to two-photon branching ratio for an object of mass M_P is calculated as in reference 19 and used as a weight factor for the current event;

(v) a dimuon mass value is generated according to the corresponding Dalitz decay mass spectrum, and dimuon x and p_T values in the overall c.m. system are obtained assuming isotropic decay of the parent object in its rest frame;

(vi) the sum of weights for events satisfying $M \leq 0.6$ GeV/c^2, $x \geq 0.1$ and $p_T \leq 1.2$ GeV/c is normalized to the 608 nb *dimuon* cross section observed at 16 GeV/c and in this way the cross section for the entire Monte Carlo generated sample is defined.

The resulting x and p_T^2 behaviour is illustrated by the solid curves in Figs. 16-18. The x distribution and the corresponding $\langle p_T^2 \rangle$ correlation

---

(*) Expression (5) has continuous first and second order derivatives w.r.t. x at x = 0.

are quite well reproduced; however, as discussed above, the calculated p_T^2 distributions tend to fall below the data for $p_T \geq 0.9$ GeV/c.

The calculated dimuon mass spectra corresponding to $x \geq 0.1$ and $x \geq 0.3$ are represented by the curves of Fig. 20(b). Although the mass spectrum does broaden somewhat with increasing x, the representation of the two data samples is only fair. However several points pertaining to both the data and the calculation need to be considered:

a) in the calculation form factors have been ignored and a simple $(p)^{2\ell}$ matrix element dependence has been used with $\ell = 1$ corresponding to P-wave decay;

b) the line shapes resulting from η and ω Dalitz decay are not well known and, for example, the inclusion of vector dominance effects in the case of ω decay could result in significant broadening of the ω Dalitz mass spectrum to be subtracted, thereby slightly steepening the residual distribution;

c) the fact that the 225 GeV/c mass spectrum reaches a maximum at a higher mass than does the calculated curve may result from a combination of resolution and acceptance effects in the data; resolution has not been folded into the calculation because the relevant experimental details are not available, but it should certainly result in broadening of the mass distribution; systematic shifts to higher mass can result from coordinate sharing and mixing which tends to occur in track-finding for small opening angle configurations; finally, the trigger used in the 225 GeV/c experiment required hits in two non-adjacent hodoscope elements; this in effect imposes a minimum mass

cut-off whose value increases with increasing x of the pair; such a moving acceptance hole would tend to trim off the leading edge of a distribution such as that calculated for Fig. 20(b).

It follows that a detailed agreement between the calculated and experimental mass spectra should not be expected in the absence of better understanding of points (a)-(c).

No claim is made that the model described in this section is unique in its ability to provide a good description of the dilepton distributions. However, it does serve to illustrate the fact that the principal features of the data can be described quite well in terms of a Dalitz mechanism. Furthermore, the model can be used to make specific, quantitative predictions concerning direct photon and single lepton production in the low p_T regime. The pertinent results on these topics are presented in the remainder of this chapter.

5.4 Implications for Direct Photon Production

The Dalitz decay mechanism described in the previous section results in a two-photon mass spectrum as illustrated in Fig. 24, where corresponding $e^+e^-\gamma$ and $\mu^+\mu^-\gamma$ mass spectra are also shown. The integrated cross section values for $\gamma\gamma$, $e^+e^-\gamma$ and $\mu^+\mu^-\gamma$ are 3.16 mb, 49.5 μb and 2.30 μb respectively, however the sizeable $\gamma\gamma$ and $e^+e^-\gamma$ cross sections are rather sensitive to certain aspects of the procedure involved.

Approximately half of the $\gamma\gamma$ and $e^+e^-\gamma$ cross section results from masses less than 0.5 GeV/c^2. From Fig. 24, only a small fraction of the $\mu^+\mu^-$ data is obtained from this region, so that a more rapid fall-off toward threshold in the parent mass spectrum would significantly reduce the implied $\gamma\gamma$ and $e^+e^-\gamma$ cross section values, with little effect on the

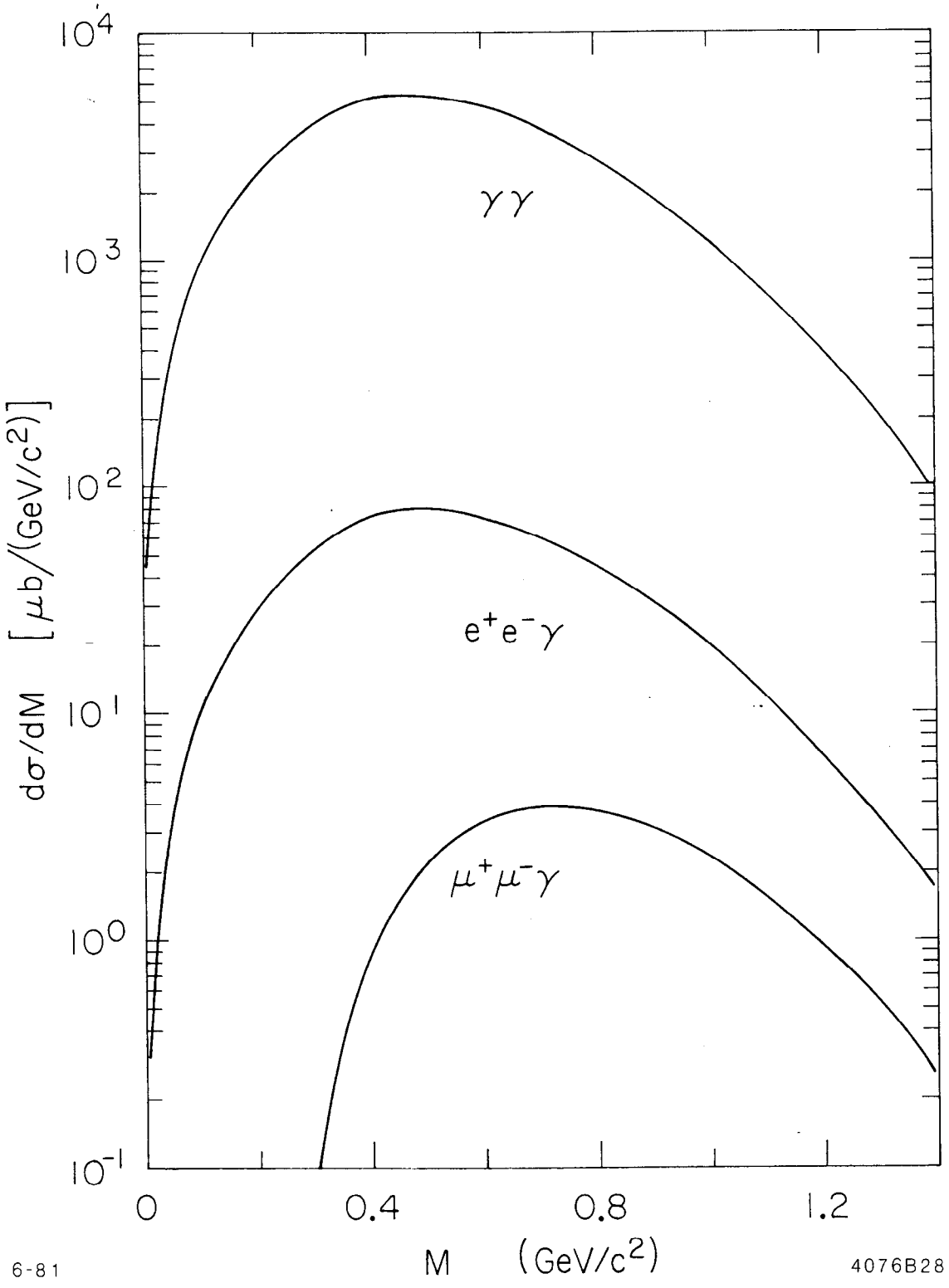

Fig. 24. The normalized $\gamma\gamma$, $e^+e^-\gamma$ and $\mu^+\mu^-\gamma$ mass spectra resulting from the model of Section 5.3.

dimuon predictions. These values are also reduced as the central mass value and σ value in expression (6) increase. However, this does broaden the resulting p_T^2 distributions for dimuons, so that large changes in these parameter values cannot be tolerated.

The role of form factors in the decay matrix element is also important. For example, the inclusion of a P-wave barrier penetration factor with a radius parameter of 1 fermi increases the dimuon branching ratio by ~50% with little effect on the dielectron rate, or on the dimuon x and p_T^2 distributions; agreement with the experimental mass distributions is improved, and the implied $\gamma\gamma$ and $e^+e^-\gamma$ cross sections are reduced by approximately one third.

The conclusion to be drawn from this is that the Dalitz mechanism described in Section 5.3 would imply the existence of a low-mass two-photon continuum at a cross section level of a few millibarns. Present experimental data cannot rule out the existence of such a continuum.

A further consequence is the existence of direct photon production at a cross section level of $\leq$5 mb.(*) A parent object with mass, x and p_T^2 distributions as described in the previous section decaying isotropically to two photons yields a photon to pion ratio with the (x, p_T) characteristics illustrated by Fig. 25. Here, the two-photon cross section is 3.16 mb and the pion data correspond to $\pi^- p \to \pi^+ X$ at 16 GeV/c.

(*) The mechanism of Fig. 22(d) does not imply a factor of two less photon production; the Kroll-Wada matrix element is reduced by a factor of two because there is only one virtual photon possibility, so that normalization to the observed dimuon cross section yields a factor of two increase in the $\pi\gamma$ cross section, i.e., essentially the same single γ cross section.

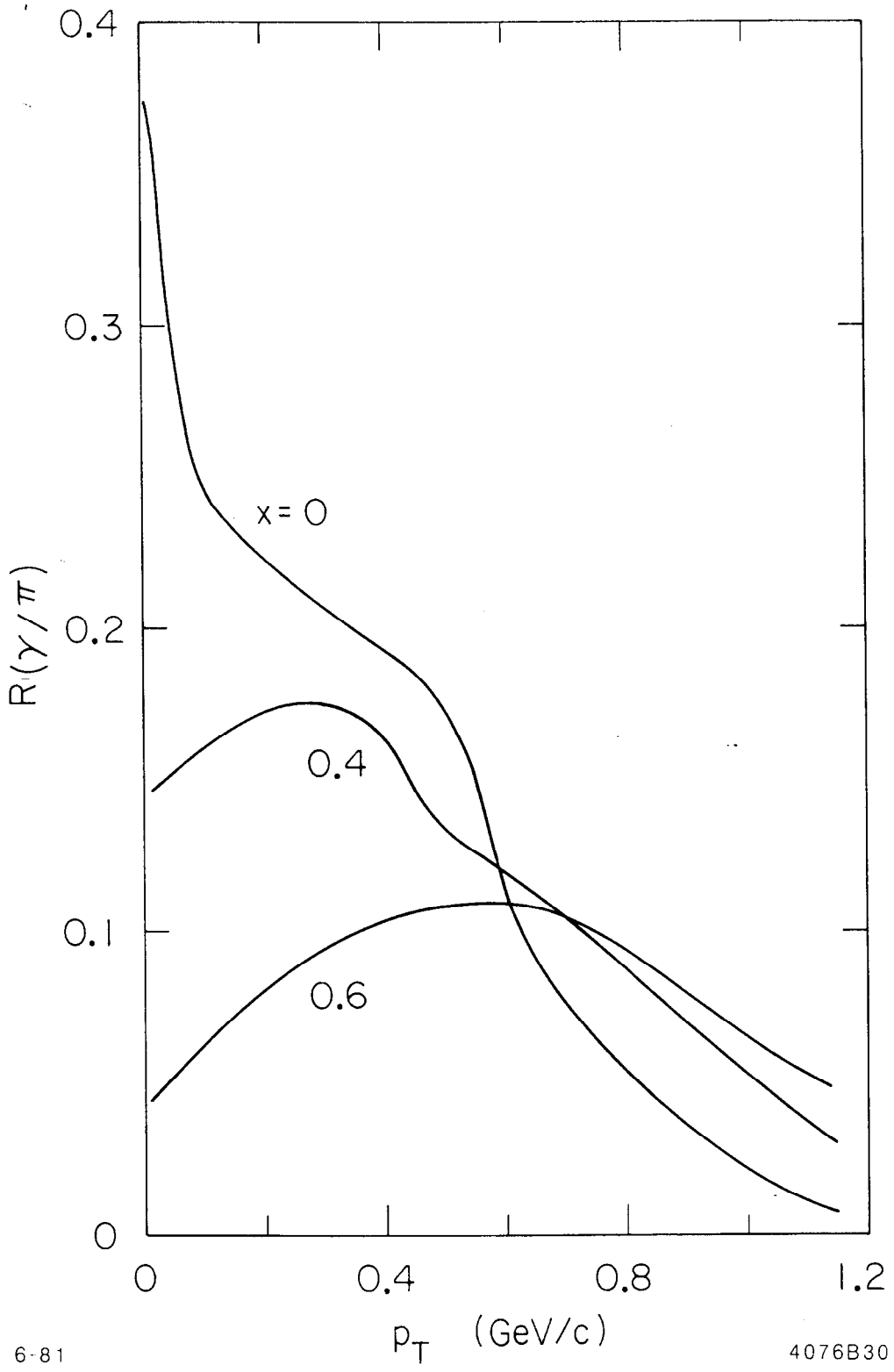

Fig. 25. The dependence on x and p_T of the γ to π ratio obtained from the model of Section 5.3.

The implication is that while the (γ/π) ratio would be at the few percent level for $p_T \sim 1$ GeV/c for all x, it may undergo very rapid increase with decreasing x and p_T, perhaps even exceeding the 10 - 20% level in the very central regions.

For the region $0.1 \leq x \leq 0.45$ and $p_T \leq 0.8$ GeV/c, the calculated direct photon cross section is 1.2 mb. This is significantly larger than the values obtained in section 3.6 by extrapolation to the photon pole. The extrapolation function, (2), corresponding to the model is roughly constant for $M \leq 0.05$ GeV/c^2, but then decreases approximately linearly up to $\sim$0.45 GeV/c^2 before flattening off at higher mass values. In Fig. 15, the first two data points lie below, and the last two data points lie above this curve; the resultant linear fit implies an extrapolation function which is slightly increasing rather than decreasing with M, thus generating the large discrepancy between the calculated and extrapolated values of the cross section. This illustrates the need for much more precise data in the low mass region.

As stated above, the two-photon cross section of $\sim$3 mb corresponds to an $e^+e^-\gamma$ cross section of $\sim$50 μb. The corresponding e^+e^- mass spectrum contains $\sim$44 μb below the π^o mass, and since the inclusive π^o Dalitz pair cross section at 16 GeV/c is $\sim$400 μb it might be thought possible to detect the presence of such a contribution by means of deviations from the expected Dalitz pair mass spectrum. The dotted curve of Fig. 26 is the mass spectrum for e^+e^- pairs resulting from the continuum, the dashed curve corresponds to π^o Dalitz decay for an inclusive π^o cross section of 35 mb, and the solid curve is the sum of the two distributions. Clearly, it would be extremely difficult to

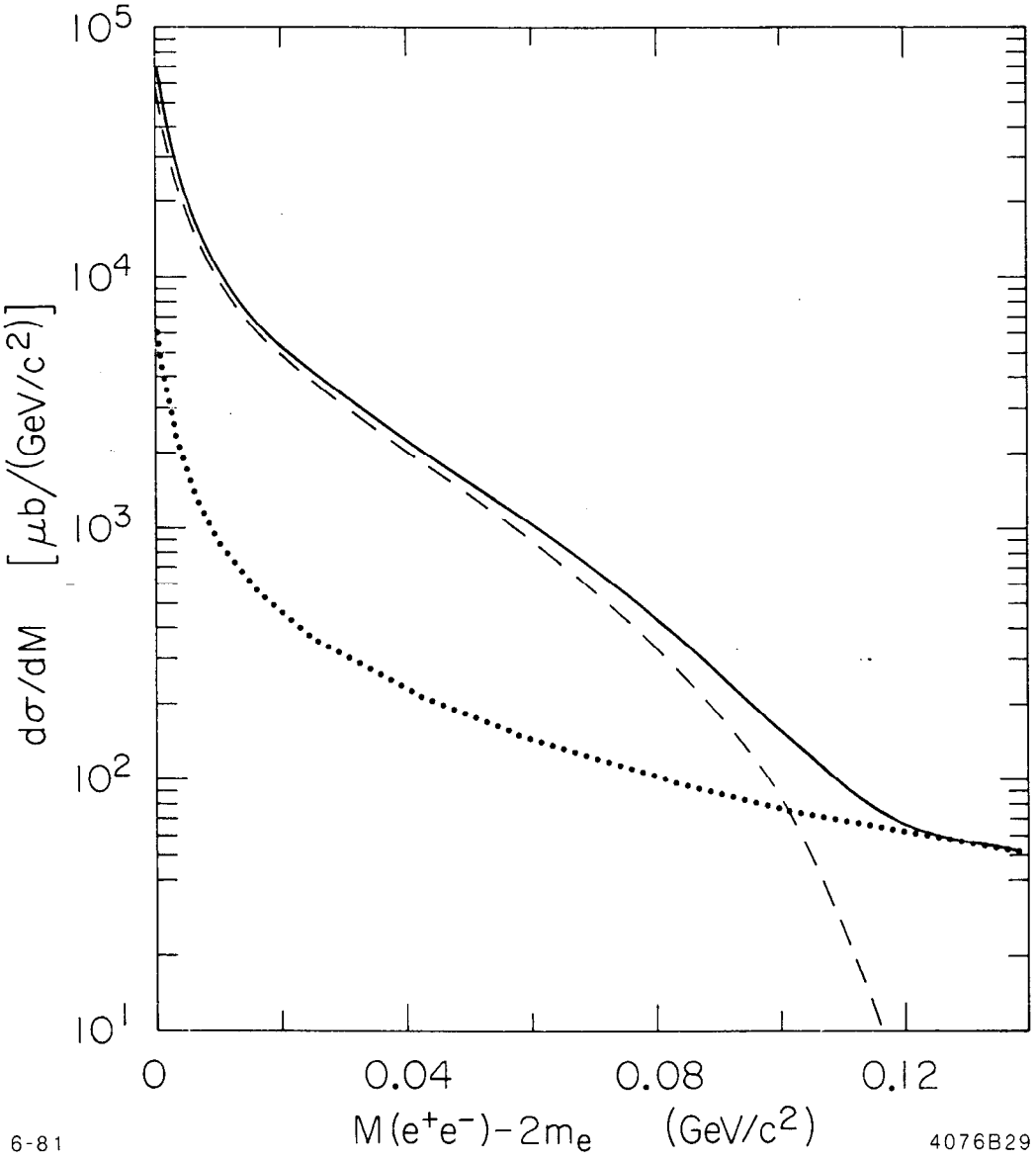

Fig. 26. The e^+e^- mass spectrum resulting from the model of Section 5.3 (dotted curve) compared with the inclusive Dalitz decay mass spectrum for inclusive π^o production at 16 GeV/c (dashed curve); the solid curve represents the sum of the two distributions.

detect the presence of such a continuum contribution by measuring only the e^+e^- spectrum; simultaneous high efficiency photon detection would be required.

5.5 Implications for Single Lepton Distributions

The model described in Section 5.3 may be used to predict the behaviour of single lepton distributions as a function of x and p_T. Dilepton decay angular distributions are generated according to (4) above, with $m = \pm 1$ in accordance with Fig. 22(b). In addition to these continuum contributions, lepton distributions resulting from η and ω Dalitz decay and from the direct decay of η, ω and ρ to two leptons are generated. The net single lepton distributions are presented in the form of lepton to pion ratios using the 16 GeV/c data on $\pi^- p \to \pi^+ X$.

The resulting (ℓ/π) ratios for πN interactions at 16 GeV/c are illustrated in Fig. 27. An extremely rapid increase in $R(e/\pi)$ is predicted at low x and low p_T. The (μ/π) ratio is also predicted to increase significantly in this region, but much less dramatically than the (e/π) ratio. In other (x, p_T) regions the ratios exhibit similar shape variations, but with $R(e/\pi)$ approximately a factor of 5 - 10 stronger than $R(\mu/\pi)$; at low p_T ($\leq$0.2 GeV/c) the ratios decrease with increasing x, whereas for $p_T \sim 1$ GeV/c they increase with increasing x.

The experimental data on $R(e/\pi)$ for $p_T \leq 1$ GeV/c result almost entirely from pp interactions at $x \sim 0$ [13(a)-(c)]. A compilation of these results is presented in Fig. 28; the data tend to increase fairly rapidly with decreasing p_T for $p_T \leq 1$ GeV/c. This behaviour is similar to that exhibited in Fig. 27 for $R(e/\pi)$ at $x = 0$, although the curve is a factor of $\sim$2 above the data for $p_T < 0.5$ GeV/c. Almost all of the

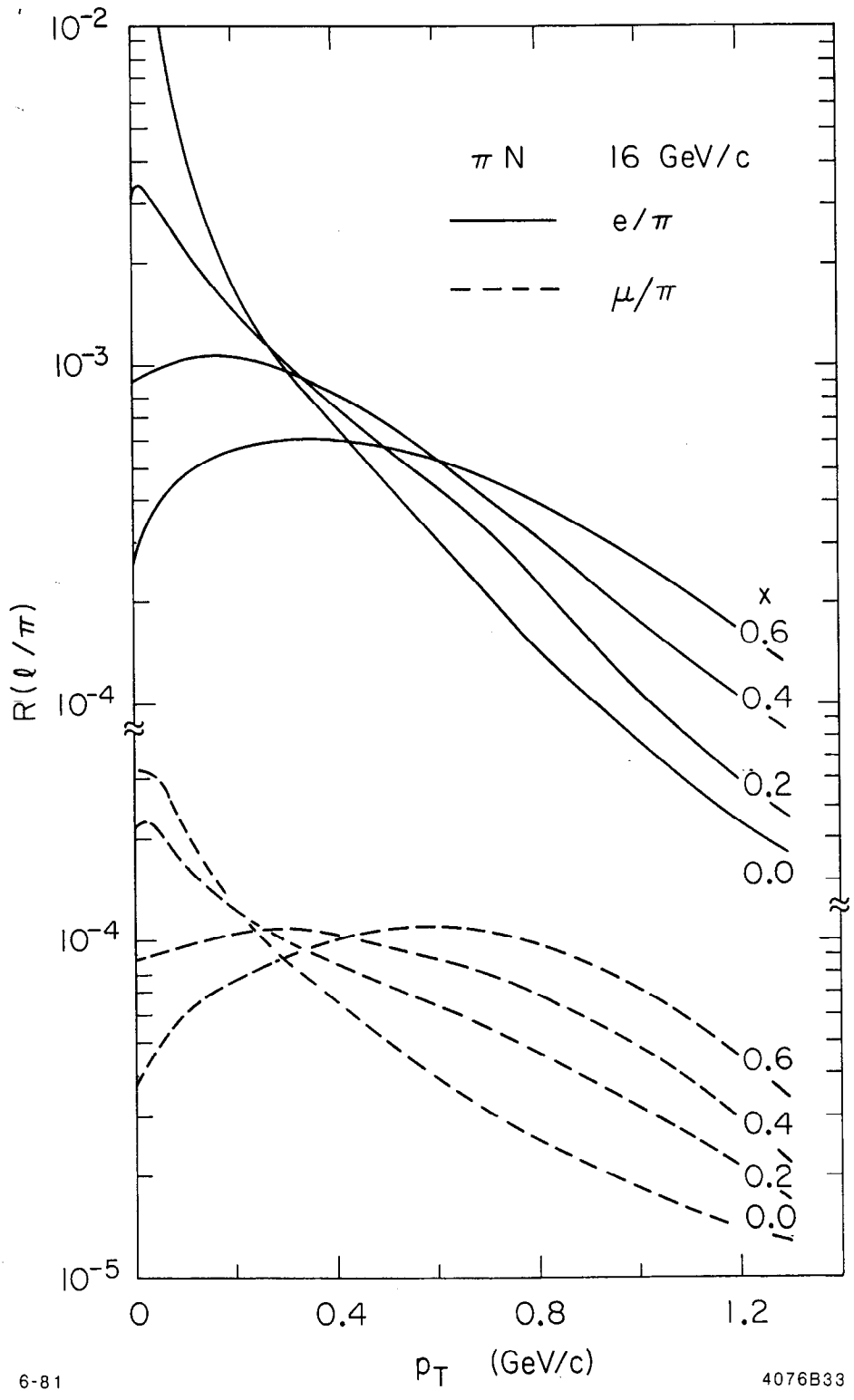

Fig. 27. The dependence of $R(e/\pi)$ and $R(\mu/\pi)$ on x and p_T for πN interactions at 16 GeV/c estimated using the model of Section 5.3 together with the contributions from η, ω and ρ decay.

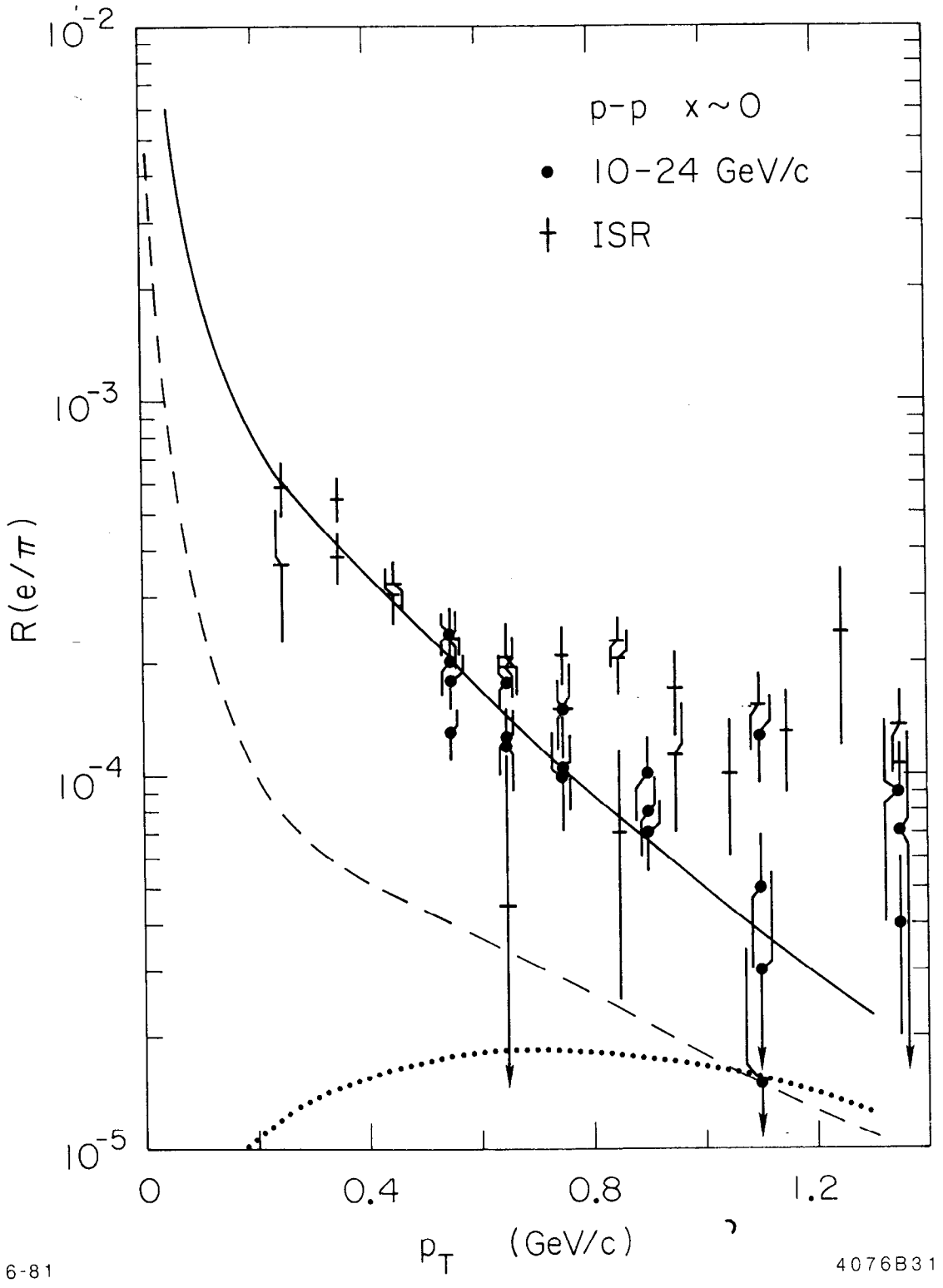

Fig. 28. The comparison of the calculated e/π ratio with a compilation of data from p-p interactions at x ~ 0; the dotted curve results from direct decay of η, ω and ρ to e^+e^-, the dashed curve from η and ω Dalitz decay and the solid curve from the model of Section 5.3 together with the resonance contributions; electrons resulting from e^+e^- pairs of mass less than 20 MeV/c^2 have been eliminated in the calculations.

data of Fig. 28 with $p_T < 1$ GeV/c result from single arm spectrometer experiments in which one and only one particle was required in the spectrometer and surrounding guard areas. This requirement amounts to a cut on e^+e^- mass and at the same time reduces the hadron counting rate. This effect is simulated in the model calculations by eliminating single electrons originating from very low mass pairs. The solid curve of Fig. 28 corresponds to a mass cut at 20 MeV/c^2, which yields a factor of ~2 reduction in $R(e/\pi)$. The dashed curve shows the contribution from η and ω Dalitz decay, while the dotted curve represents the effect of direct η, ω and ρ decay to e^+e^-. If the mass cut were increased to 60 MeV/c^2 a further factor of two reduction would result. Clearly, the solid curve of Fig. 28 describes the behaviour of $R(e/\pi)$ for $p_T \leq 1$ GeV/c rather well. At higher p_T the measurements appear to flatten off at a value of $\sim 10^{-4}$; as discussed previously, the results from the model would be expected to be below the data in this region and serious comparison should not be attempted.

The data on $R(\mu/\pi)$ for $p_T < 1$ GeV/c are obtained from p - N interactions in the 200 - 400 GeV/c incident momentum range [13(d)-(g)], and correspond to integrals over p_T at forward x values. A compilation of these data(*) is presented in Fig. 29(b).

The behaviour of $R(\ell/\pi)$ integrated over p_T is shown by the dashed curves of Fig. 29; the model calculation results and the contributions from η, ρ and ω decay have been combined, and it is evident that the dashed curve of Fig. 29(b) does not agree at all well with the measurements.

(*) The data are presented as $(\mu^+ + \mu^-)/(\pi^+ + \pi^-)$ where appropriate.

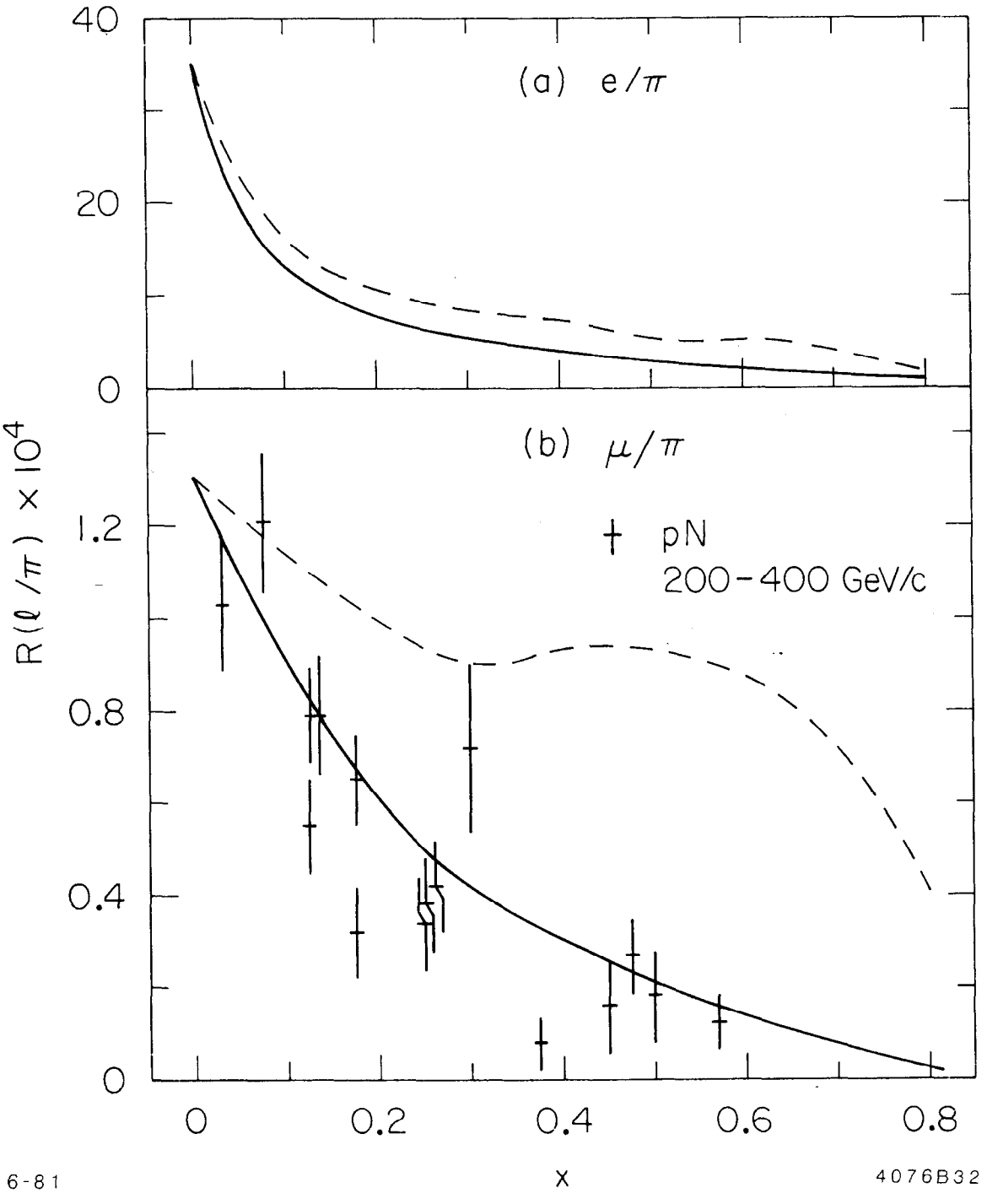

Fig. 29. The calculated x dependence of the ℓ/π ratio integrated over $p_T \leq 1$ GeV/c; the dashed curves represent the sum of the model contribution and that from forward resonance production in π^-p interactions at 16 GeV/c; the solid curves result from the model and the contribution from backward resonance production at 16 GeV/c; the data of Fig. 29(b) correspond to pN interactions in the range 200 - 400 GeV/c incident momentum.

However, inclusive ρ^o production in pp interactions at 24 GeV/c [40] agrees very well with backward production of ρ^o in π^-p interactions at 16 GeV/c [16a]. Consequently, the solid curves of Fig. 29 are generated by combining the model calculation results (which are forward-backward symmetric by construction) with the corresponding backward hemisphere contributions from η, ω and ρ^o decay. In this regard it should be noted that the inclusive π^+ cross section for π^-p interactions at 16 GeV/c is approximately forward-backward symmetric and the denominator in $R(\ell/\pi)$ is obtained as the average of the forward and backward cross sections.

The resulting curve of Fig. 29(b) describes the data very well. In addition, the value of $R(\mu/\pi)$ integrated over the entire forward hemisphere is quoted as $(0.93 \pm 0.13) \times 10^{-4}$ in reference 13(g); the solid curve of Fig. 29(b) integrates to a value of 0.78×10^{-4} for the forward hemisphere, and it is known that at 350 GeV/c incident momentum [13(g)] there are additional contributions, for example from the decay of charmed particles, which tend to increase $R(\mu/\pi)$.

It follows from this that the dashed curves of Fig. 29 should be considered estimates of the behaviour of $R(\mu/\pi)$ in the forward hemisphere for πN interactions and that the solid curves describe the behaviour expected for pN interactions and in the backward hemisphere for πN interactions. The corresponding x and p_T dependence of $R(\ell/\pi)$ for pN interactions is shown in Fig. 30. The general characteristics are similar to those of Fig. 27 (the distributions for $x = 0$ are the same by construction, but the decrease of $R(\ell/\pi)$ at low p_T with increasing x is more rapid for

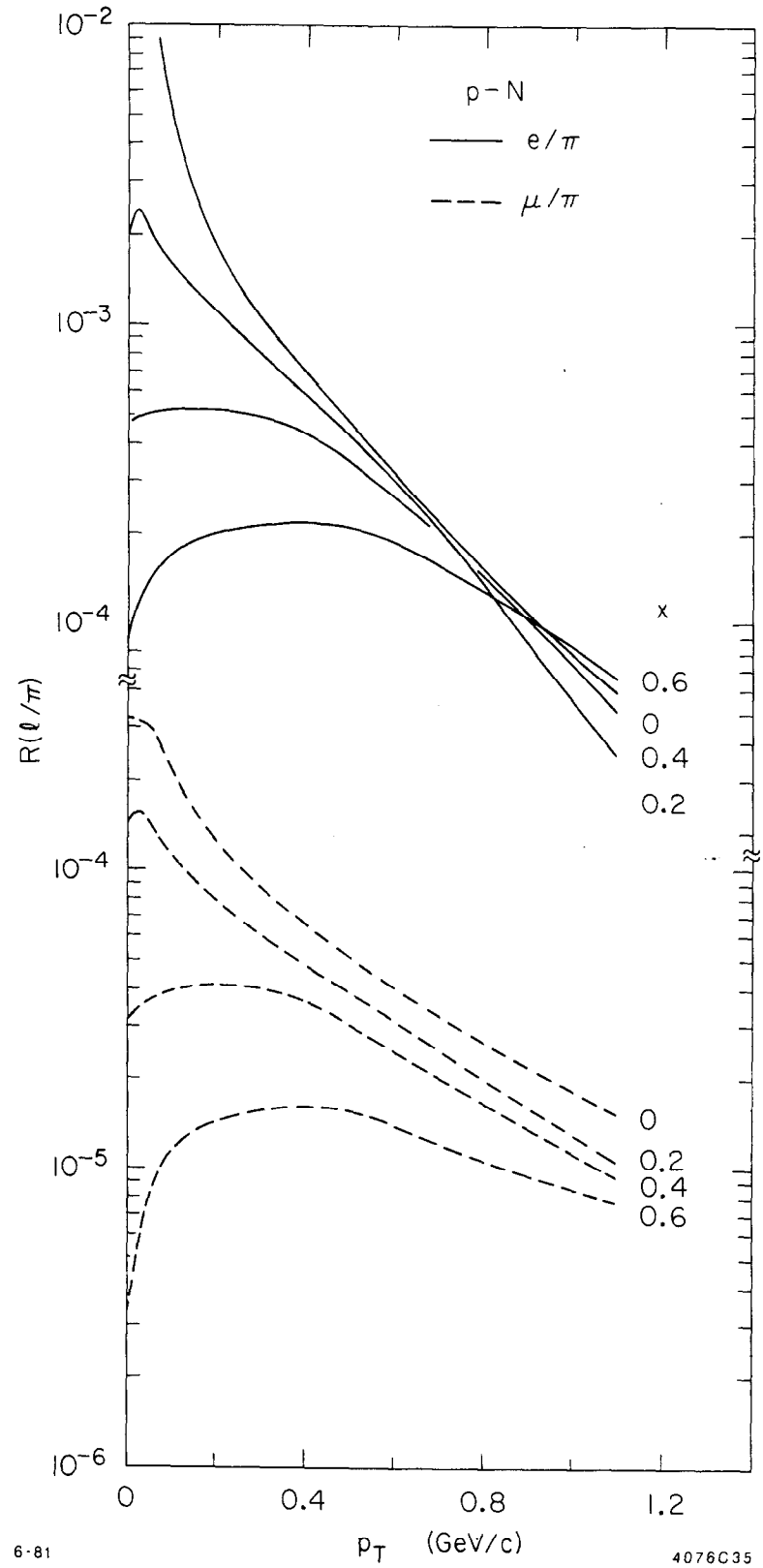

Fig. 30. The (x, p_T) dependence of $R(\ell/\pi)$ for pN interactions calculated as for Fig. 27, but using the contributions from backward η, ω and ρ production at 16 GeV/c.

pN interactions; $R(e/\pi)$ is approximately independent of x for $p_T \sim 1$ GeV/c, whereas $R(\mu/\pi)$ decreases with increasing x in this region.

Finally, in Fig. 31 the expected behaviour of $R(e/\mu)$ with x and p_T is summarized for forward πN and pN interactions. The calculated curve for $x = 0$ is the same in both cases, and exhibits steady increase for p_T less than 1 GeV/c down to ~0.2 GeV/c, with extremely rapid increase thereafter. This sharp increase is highly localized to $x \sim 0$. At low p_T, $R(e/\mu)$ decreases with increasing x for πN, but is essentially flat for pN interactions; for $p_T \sim 1$ GeV/c the πN ratio should be approximately x-independent, whereas the pN ratio would be expected to increase with x.

In summary, the simple model described in Section 5.3 is able to provide a good, simultaneous quantitative description of the experimental data on $R(e/\pi)$ and $R(\mu/\pi)$ in the region $p_T \lesssim 1$ GeV/c when the additional contributions resulting from η, ω and ρ decay are taken correctly into account.

6. Conclusions

The production of direct e^+e^- pairs has been measured in the region $0.10 < x \leq 0.45$, $p_T^2 \leq 0.64$ $(GeV/c)^2$ and $0.2 \leq M \leq 1.2$ GeV/c^2. A low mass continuum in excess of the direct or Dalitz decay of known resonances is observed for $0.2 \leq M \leq 0.7$ GeV/c^2. This continuum corresponds to a cross section of 700 ± 180 nb, and exhibits very steep x and p_T^2 distributions suggesting a central production mechanism; the steepness of the low p_T^2 spike appears to be increasing with decreasing x.

For the accessible region of phase space, the $(e^+e^-/\pi^+\pi^-)$ ratio is $(4.7 \pm 1.2) \times 10^{-5}$ after subtracting known resonance contributions

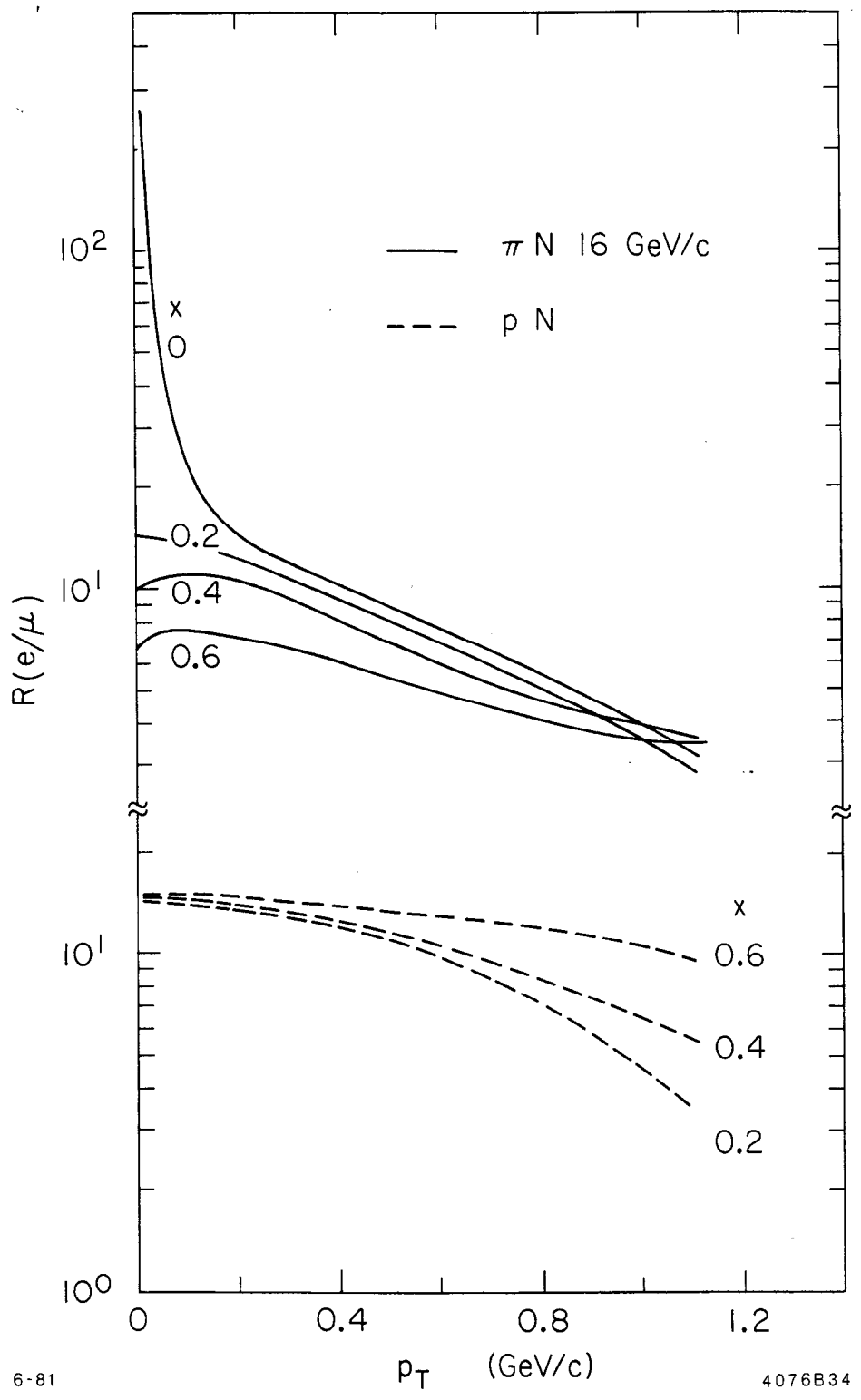

Fig. 31. The estimated dependence on x and p_T of R(e/μ) for πN and pN interactions; the pN distribution for x = 0 is the same as the πN distribution.

from the numerator. However, the ratio exhibits strong x and p_T^2 dependence.

The cross section for direct photon production in the acceptance region of the experiment is estimated to be $\sigma_\gamma = 386 \pm 95$ μb assuming a constant extrapolation function, and $\sigma_\gamma = 240 \pm 350$ μb if a linear M-dependence is allowed; the corresponding γ/π ratios are estimated to be $(5.2 \pm 1.3)\%$ and $(3.2 \pm 4.7)\%$ respectively.

The e^+e^- data from the present experiment are found to be quite compatible with dimuon data at 16 GeV/c when effects due to the electron-muon mass difference are taken into account. The combined data are considered to provide information on dimuon production for $x \geq 0.1$ and $p_T \leq 1.2$ GeV/c and yield a cross section of 864 ± 124 nb in this region for *dimuon* masses less than 0.6 GeV/c^2. After subtraction of estimated contributions from η and ω Dalitz decay, a residual continuum cross section of 608 ± 135 nb is obtained. The corresponding x distribution is approximately exponential with slope 6.3 ± 0.1, and there exists a pronounced $(x, \langle p_T^2 \rangle)$ correlation in the data. Similar behaviour is found for loss mass dimuon data from πC interactions at 225 GeV/c in the region $x \geq 0.07$, although in this case the residual x distriubtion is much steeper and has slope ~15.9. Although the integrated p_T^2 distributions at 16 and 225 GeV/c are similar in shape, the $(x, \langle p_T^2 \rangle)$ correlation appears different at the two energies. The continuum mass distribution at 16 GeV/c for $x \geq 0.3$ appears broader than that observed for $x \geq 0.07$ at 225 GeV/c, indicating the existence of a possible (M, x) correlation.

A simple model based on the Dalitz-like decay of a $q\text{-}\bar{q}$ continuum is able to describe the principal features of the 16 GeV/c dilepton data quite well.

The implications for direct photon production have been considered and it has been conjectured that a low mass diphoton continuum may exist at the level of a few millibarns of cross section. The corresponding single photon cross section should yield $R(\gamma/\pi)$ behaviour which grows rapidly from a few percent for $p_T \sim 1$ GeV/c to the 10 - 20% level at low x and low p_T.

Finally the implications for the behaviour of the single lepton to pion ratio have been considered in some detail in comparison with the experimental data for $p_T \leq 1$ GeV/c. It has been shown that the proposed mechanism, together with the contributions from η, ρ and ω decay, is able to simultaneously describe the $R(e/\pi)$ behaviour with p_T for $x \sim 0$ and the $R(\mu/\pi)$ behaviour with x when integrated over p_T. Predictions of the behaviour over the entire (x, p_T) plane have been presented for πN and pN interactions and the sensitivity of the πN results to the pronounced forward-backward asymmetry of η, ω and ρ production has been demonstrated.

Further experiments are clearly required in order to test the conjectures presented in this paper as they concern low mass dilepton and single lepton production. These experiments should set as their goal the simultaneous measurement and efficient detection of leptons and photons, for it is only in this way that contributions from π^o, η and ω Dalitz decay can be removed reliably in order to reveal the nature and origin of the low mass dilepton continuum.

Acknowledgments

We are grateful to R. Bierce, R. Carnegie, M. Ferro-Luzzi, H. Jensen, A. Kilert, D. McShurley, J. Pine, and W. Walsh for their help at various states of the experiment. The loan of the shower counters used in the experiment from SLAC Group E is acknowledged. We should also like to thank Dr. Kelby Anderson of the Chicago-Princeton collaboration for making available to us unpublished data on dimuon production at 225 GeV/c.

[1] For reviews see e.g., N. S. Craigie, Phys. Rep. 47 (1978) 1, R. Stroynowski, Phys. Rep. 71 (1981) 1.

[2] S. D. Drell and T. M. Yan, Phys. Rev. Lett. 25 (1970) 316; Ann. Phys. 66 (1971) 578.

[3] K. J. Anderson et al., Phys. Rev. Lett. 37 (1976) 799.

[4] W. M. Morse et al., Phys. Rev. D18 (1978) 3145; D. M. Grannan et al., Phys. Rev. D18 (1978) 3150.

[5] J. Alspector et al., Phys. Lett. 81B (1979) 397.

[6] K. Bunnell et al., Phys. Rev. Lett. 40 (1978) 136; B. Haber et al., Phys. Rev. D22 (1980) 2107; R. Cassell, private communication.

[7] A Chilingarov et al., Nucl. Phys. B151 (1979) 29.

[8] J. H. Cobb et al., Phys. Lett. 78B (1978) 519.

[9] J. Ballam et al., Phys. Rev. Lett. 41 (1978) 1207.

[10] J. Guy et al., Phys. Lett. 66B (1977) 300.

[11] R. Barloutaud et al., Nucl. Phys. B176 (1980) 285.

[12] G. Levman et al., Phys. Rev. D21 (1980) 1.

[13] a) F. W. Busser et al., Phys. Lett. 53B (1974) 212; Nucl. Phys. B113 (1976) 189;

b) L. Baum et al., Phys. Lett. 60B (1976) 485; M. Barone et al., Nucl. Phys. B132 (1978) 29.

c) E. W. Beier et al., Phys. Rev. Lett. 37 (1976) 1117;

d) D. Bucholz et al., Phys. Rev. Lett. 36 (1976) 932;

e) H. Kasha et al., Phys. Rev. Lett. 36 (1976) 1007;

f) J. G. Branson et al., Phys. Rev. Lett. 38 (1977) 457;

g) J. L. Ritchie et al., Phys. Rev. Lett 44 (1980) 230;
K.W.B. Merritt et al., to be published.

[14] R. Stroynowski et al., Phys. Lett. 97B (1980) 315.

[15] a) D. L. Blockus, Ph.D. Thesis, The Johns Hopkins Univ. (1980);
b) M. Marshall, Ph.D. Thesis, California Institute of Technology (1979);
c) C. L. Woody, Ph.D. Thesis, The Johns Hopkins Univ. (1978);
d) M.G.D. Gilchriese, Ph.D. Thesis, Stanford Univ., SLAC-202 (1977).

[16] a) J. Bartke et al., Nucl. Phys. B107 (1976) 93;
b) J. Bartke et al., Nucl. Phys. B118 (1977) 360.

[17] We are grateful to Dr. D.R.O. Morrison and the Aachen-Berlin-Bonn-CERN-Cracow-Heidelberg-Warsaw Collaboration for providing their 16 GeV π^-p data, which were instrumental to these Monte Carlo Studies.

[18] N. Barash-Schmidt et al., Particle Data Tables, Phys. Lett. 75B (1978) 1.

[19] N. M. Kroll and W. Wada, Phys. Rev. 98 (1955) 1355; T. Miyazaki and E. Takasugi, Phys. Rev. D8 (1973) 2051.

[20] C. H. Lai and C. Quigg, FNAL Report No. FN-296 (1976).

[21] G. R. Farrar and S. C. Frautschi, Phys. Rev. Letters 36 (1976) 1017.

[22] For detailed derivation see W. Dunwoodie, SLAC Group B, E-127 Notes (1980).

[23] G. Abshire et al., "Anomalous Low Mass e^+e^- Pair Production in 17 GeV/c π^-p Collisions," submitted to the XXth International Conference on High Energy Physics, Madison, Wisconsin (1980).

[24] There is a hole in the acceptance of the present experiment for $0.8 \leq p_T \leq 1.2$ GeV/c and $0.10 \leq x \leq 0.15$, however, the loss of cross section in extending the p_T range to 1.2 GeV/c is very small.

[25] Throughout this paper ω Dalitz decay is calculated ignoring vector dominance; its inclusion results in a reduction of the excess continuum cross section by $\sim$50 nb.

[26] G. G. Henry, Ph.D. Thesis, Enrico Fermi Institute, Univ. of Chicago (1978).

[27] J. G. Branson et al., Phys. Rev. Lett. 38 (1977) 1334.

[28] K. J. Anderson, private communication.

[29] K. J. Anderson et al., Phys. Rev. Lett. 37 (1976) 803.

[30] C. B. Newman et al., Phys. Rev. Lett. 42 (1979) 951.

[31] J. D. Bjorken and H. Weisberg, Phys. Rev. D13 (1976) 1405.

[32] V. Cerny et al., Phys. Lett. 70B (1977) 61; Acta Phys. Pol. B9 (1978) 901.

[33] V. Cerny et al., Acta Phys. Pol. B10 (1979) 537.

[34] a) G. R. Farrar and S. C. Frautschi, Phys. Rev. Lett. 36 (1976) 1017;

b) R. Ruckl, Phys. Lett. 64B (1976) 39;

c) N. S. Craigie and H. N. Thompson, Nuc. Phys. B141 (1978) 121.

[35] a) E. L. Feinberg, Nuovo Cimento 34A (1976) 391;

b) E. V. Shuryak, Phys. Lett. 78B (1978) 150.

[36] T. Goldman et al., Phys. Rev. D20 (1979) 619.

[37] C. Field, private communication.

[38] The dotted curve of Fig. 18 was generated by treating inclusive π^+'s from π^-p interactions at 16 GeV/c as π^o's and generating the corresponding Dalitz decay products; this procedure results in a very good description of the x and p_T dependence of the actual 18 GeV/c Dalitz pair data.

[39] R. J. Oakes, Nuovo Cimento 44 (1966) 440.

[40] V. Blobel et al., Phys. Lett. 48B (1974) 73.